Abell 1367: a high fraction of late-type galaxies displaying H I morphological and kinematic perturbations

T. C. Scott,[1,2]★ E. Brinks,[2] L. Cortese,[3] A. Boselli[4] and H. Bravo–Alfaro[5]

[1]*Institute of Astrophysics and Space Sciences (IA), Rua das Estrelas, P-4150–762 Porto, Portugal*
[2]*Centre for Astrophysics Research, University of Hertfordshire, College Lane, Hatfield AL10 9AB, UK*
[3]*International Centre for Radio Astronomy Research, The University of Western Australia, 7 Fairway, 6009, Crawley WA, Australia*
[4]*Aix Marseille Université, CNRS, LAM (Laboratoire d'Astrophysique de Marseille) UMR 7326, F-13388 Marseille, France*
[5]*Departamento de Astronomía, Universidad de Guanajuato, Apdo. Postal 144, Guanajuato 36000, Mexico*

ABSTRACT

To investigate the effects the cluster environment has on late-type galaxies (LTGs), we studied H I perturbation signatures for all Abell 1367 LTGs with H I detections. We used new Very Large Array H I observations combined with AGES single-dish blind survey data. Our study indicates that the asymmetry between the high- and low-velocity wings of the characteristic double-horn-integrated H I spectrum as measured by the asymmetry parameter, A_{flux}, can be a useful diagnostic for ongoing and/or recent H I stripping. 26 per cent of A1367 LTGs have an A_{flux} ratio, more asymmetrical than 3 times the 1σ spread in the A_{flux} ratio distribution of an undisturbed sample of isolated galaxies (2 per cent) and samples from other denser environments (10 per cent–20 per cent). Over half of the A1367 LTGs, which are members of groups or pairs, have an A_{flux} ratio larger than twice the 1σ spread found in the isolated sample. This suggests intergroup/pair interactions could be making a significant contribution to the LTGs displaying such A_{flux} ratios. The study also demonstrates that the definition of the H I offset from the optical centre of LTGs is resolution dependent, suggesting that unresolved AGES H I offsets that are significantly larger than the pointing uncertainties ($>2\sigma$), reflect interactions which have asymmetrically displaced, significant masses of lower density H I, while having minimal impact on the location of the highest density H I in resolved maps. The distribution of A_{flux} from a comparable sample of Virgo galaxies provides a clear indication that the frequency of H I profile perturbations is lower than in A1367.

Key words: galaxies: clusters: individual: (Abell 1367) – galaxies: clusters: intracluster medium – galaxies: evolution – galaxies: ISM – galaxies: interactions.

1 INTRODUCTION

Since at least $z \simeq 0.5$ mechanisms have operated within the galaxy cluster environment to transform late-type galaxies (LTGs) into S0 Hubble types (Fasano et al. 2000; Goto et al. 2003). A number of different mechanisms have been proposed with the principle ones being stripping of the interstellar medium (ISM) by interaction with the diffuse intracluster medium (ICM), as originally proposed by Gunn & Gott (1972; primarily ram-pressure stripping) and tidal interactions. In clusters tidal interactions divide into two main types: repeated low impact high-velocity 'harassment' interactions near the cluster core (Moore et al. 1996) and higher impact lower velocity 'pre-processing' interactions amongst members of infalling groups (Dressler 2004). To date, it is unclear whether the same mechanism is dominant at all cluster radii, in all cluster types and at all redshifts

(Domínguez, Muriel & Lambas 2001; Dressler 2004; Boselli & Gavazzi 2006; Poggianti et al. 2009; Boselli et al. 2014).

An important aspect of these questions is the mechanism removing cold neutral gas (H I and molecular gas) from cluster LTGs. At low z ($\lesssim 0.1$), the fraction of H I deficient galaxies[1] in galaxy clusters rises towards the cluster centres (Solanes et al. 2001; van Gorkom 2004). Koopmann & Kenney (2004), Boselli et al. (2006), and Cortese et al. (2012) showed that the H I deficiencies in cluster LTGs correlate with the truncation of their star forming and dust discs. This implies progressive outside–in H I disc truncation is responsible for a corresponding quenching of star formation. X-ray emission from the ICM in clusters typically shows that ICM densities rise steeply towards cluster cores and models predict that

---

★E-mail: tom.scott@astro.up.pt

[1] A galaxy's H I deficiency is defined as the log of the ratio of the expected to observed gas mass (Haynes & Giovanelli 1984). Negative values indicate an H I excess over the expected content.

ram-pressure stripping will reach its maximum efficiency when a galaxy transits the high-density ICM in the cluster core region (Roediger & Hensler 2005; Tonnesen 2007). A number of low redshift ($z \lesssim 0.2$) resolved H I studies explain truncated H I discs and H I deficiencies of LTGs projected within ∼1 Mpc of nearby cluster ICM cores as arising from ram-pressure stripping (e.g. Bravo-Alfaro et al. 2000; Vollmer et al. 2008; Chung et al. 2009; Jaffé et al. 2015; Yoon et al. 2017). Deep narrow band Hα imaging studies revealed long Hα tails near the cores of several nearby clusters (e.g. Gavazzi et al. 2001b; Boselli et al. 2014, 2016; Fossati et al. 2016; Yagi et al. 2017) and these are usually also attributed to ram-pressure stripping. The typical absence of evidence of tidally perturbed old stellar discs in these and other studies have led, along with other circumstantial evidence, to a consensus view that ram-pressure stripping is the dominant mechanism accelerating the evolution of LTGs in nearby clusters (Boselli & Gavazzi 2006; Boselli et al. 2014). However, the density of galaxies also increases towards the clusters cores so 'harassment' (Moore et al. 1996) might also be involved in depleting and truncating the H I discs. H I observational evidence for harassment is quite limited (one example being Haynes, Giovanelli & Kent 2007), but the concentration of intracluster light near the centres of clusters is consistent with such a tidal mechanism (e.g. Montes & Trujillo 2014). An alternative explanation is that the H I removal and morphology transformations occur in the cluster outskirts as a result of group 'pre-processing' tidal interactions (Dressler 2004), prior to the LTGs arriving in the core region of clusters, e.g. the Blue Infalling Group (Cortese et al. 2006), and in the outskirts of Abell 1367 and RSCG 42 (Scott et al. 2012). Studies of group galaxies confirm that their H I content and distribution are impacted by the group environment (Hess & Wilcots 2013; Brown et al. 2017). It is already clear that multiple H I removal mechanisms can operate simultaneously in individual galaxies and clusters. But, particularly beyond the virial radius, the relative importance of each type of mechanism remains controversial. For example, modelling by Tonnesen (2007) claims ram-pressure effects can extend to three virial radii, whereas modelling by Bekki (2014) indicates that a Milky Way mass spiral might not be fully stripped of its H I during a transit though a Virgo mass ICM core.

Abell 1367 ($z = 0.02$) is a dynamically young spiral-rich galaxy cluster with an X-ray luminosity 1.25×10^{44} erg s^{-1} (Plionis, Tovmassian & Andernach 2009). The cluster's total mass is ∼6.9×10^{14} M$_{\odot}$ (Boselli & Gavazzi 2006), about half that of Coma. Its two subclusters (SE and NW) are in the early stages of an approximately equal mass merger, about 200 Myr from core contact (Donnelly et al. 1998). Cortese et al. (2004) reported the cluster velocity as 6484 ± 81 km s^{-1} and established that each subcluster has its own substructure. The majority of a sample of bright LTGs projected within a radius of 1 Mpc from the cluster centre and two groups near the virial radius have H I and/or molecular gas signatures indicating that they are suffering recent or ongoing interactions, which have strongly impacted their ISM (Gavazzi & Jaffe 1987; Gavazzi 1989). A common signature being a larger than expected offset between H I and optical intensity maxima, referred to hereafter as an H I offset (Scott et al. 2010, 2012, 2013, 2015, papers I, II, III, and IV, respectively from here onwards).

In this paper, we report on observations with the NRAO[2] Karl G. Jansky Very Large Array (VLA) in its C configuration (∼15 arcsec

resolution) mapping 15 A1367 LTGs and an extragalactic H II region (referred to from now on as the C-array detections). From the cumulatively available H I data for A1367 LTGs, we investigate four H I disc perturbation signatures (resolved and unresolved H I offsets, the asymmetry in the H I spectral profiles as well as optical/H I velocity offsets) and their relation to selected galaxy and cluster properties. An important aspect was to improve the understanding of the relation between the perturbation signatures revealed by single-dish and resolved H I observations. Disturbances to an LTGs virialized and regularly rotating H I disc can produce asymmetric signatures in its 1D H I profile and/or 2D H I velocity field. Either of the signatures provides evidence of perturbed H I. The paper also addresses the question of whether or not the cumulative H I data now available support the earlier indications, from Paper I that the frequency of LTGs with perturbed H I is abnormally high in A1367.

We utilize Arecibo single dish (AGES[3] and ALFALFA[4]) and our own VLA H I data together with optical data from NED[5] and Hyperleda[6] as well as SDSS[7] and archived X-ray data from *ROSAT* and *XMM –Newton* for A1367 from The High Energy Astrophysics Science Archive Research Center. We also used *Spitzer*, *WISE*,[8] GOLDMine[9] and 2MASS[10] near-infrared (NIR) as well as *GALEX*[11] ultraviolet (UV) archive data. Section 2 gives details of the VLA C-array observations with the VLA results given in Section 3. Section 4 describes the H I data used in the H I offset and spectral profile analysis set out in Section 5.3. A discussion follows in Section 5 with concluding remarks in Section 6. Based on a redshift to A1367 of 0.022 and assuming $\Omega_M = 0.3$, $\Omega_\Lambda = 0.7$, and $H_o = 72$ km s^{-1} Mpc^{-1} (Spergel et al. 2007), the distance to the cluster is 92 Mpc and the angular scale is 1 arcmin ∼24.8 kpc. All α and δ positions referred to throughout this paper are J2000.0.

2 OBSERVATIONS

We observed H I in three fields using the VLA in C-array configuration. The full width at half power (FWHP) primary beams (∼32 arcmin) of all three fields are projected well within the 104 arcmin (2.58 Mpc) virial radius of the cluster (Moss 2006). The VLA FWHP beams and velocity ranges are fully within the A1367 volume of the AGES blind single-dish H I survey (Cortese et al. 2008). The observations were made in correlator mode 4 which gave two independent intermediate frequencies (IFs), each with dual polarization (right- and left-hand circulars). With the exception of field B, the IFs for each field's observations were set up so that each IF generated a position–position–velocity cube (α, δ, and velocity) with a ∼ 500 km s^{-1} velocity range, with the velocity ranges of the two cubes set adjacent to each other with a small velocity overlap. Where H I for the same target was detected in more than one IF, cubes with adjacent contiguous velocities were combined, using the AIPS task MCUBE, to produce a cube for the field with a velocity range of ∼1000 km s^{-1}. The observations and final cubes had a velocity resolution of ∼11 km s^{-1}. Fig. 1 indicates the

---

[2] The National Radio Astronomy Observatory is a facility of the National Science Foundation operated under cooperative agreement by Associated Universities, Inc.

[3] Arecibo Galaxy Environment Survey.

[4] The Arecibo Legacy Fast ALFA survey.

[5] NASA/IPAC Extragalactic Database.

[6] Hyperleda (Makarov et al. 2014, http://leda.univ-lyon1.fr).

[7] Sloan Digital Sky Survey.

[8] Wide-field Infrared Survey Explorer.

[9] Galaxy Online Database Milano Network (Gavazzi et al. 2003, http://goldmine.mib.infn.it/).

[10] Two Micron All Sky Survey (Skrutskie et al. 2006).
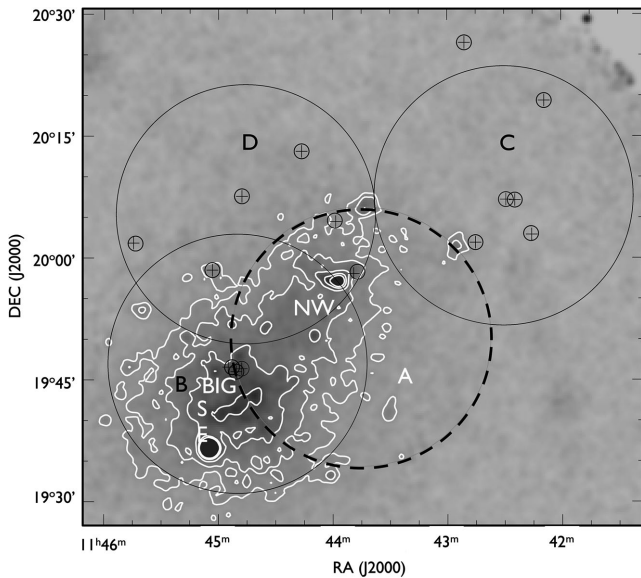
[11] Galaxy Evolution Explorer.

Figure 1. A1367:theFWHP (32 arcmin) primary beams for the three VLA fields (B, C, and D) are indicated with large black circles. The primary beam of the VLA D-array observations (field A) reported in Paper I is shown with a dashed circle for reference. The H I positions of our VLA C-array H I detections from fields B, C, and D are shown with small black circles, the positions of their optical counterparts shown with black crosses. The grey scale is a *ROSAT* X-ray image with white contours overlaid. The projected positions of the SE, NW subclusters, and the BIG compact group are labelled.

FWHP primary beams for the three pointings with large circles. The figure also shows the intensity of the X-ray emission (*ROSAT*; Donnelly et al. 1998) from the cluster's ICM (white contours) and the positions of the VLA C-array H I detections (small black circles enclosing crosses). Observational parameters for the three fields are listed in Table 1, including the velocity resolution, central velocities, and the rms noise per channel.

Sensitivity is non-uniform between the VLA fields because of their differing integration times. Additionally, for all fields, there is a sharp drop in sensitivity beyond the primary beam FWHP radius. We applied the AIPS task PBCOR to the cubes to correct for this. Consequently, the H I flux density for SDSS J114250.97+202631.8, which is projected beyond the FWHP of the Field C primary beam, is more uncertain than for the other C-array detections.

Our observations were carried out under dynamic scheduling between 2008 April 14 and May 30. All of the observations were made during the period in which the VLA antennas were being systematically upgraded to 'EVLA[12]-standard' antennas. During the observations, the array consisted of approximately equal numbers VLA and EVLA antennas. As a result, the observations were significantly impacted by transition effects. The data were calibrated and imaged with the AIPS software package, but the standard calibration and reduction procedures had to be modified to overcome a number of issues associated with the VLA–EVLA transition. In particular, all EVLA–EVLA baselines were discarded and the bandpass calibration was carried out as the first step of the calibration rather than at the end as is usual. The observations were made without online Doppler tracking or Hanning smoothing. This required post-observation correction for changes in Doppler shifts during

___

[12] Expanded Very Large Array also known as the Karl G. Jansky Very Large Array.

the observations and Hanning smoothing using the AIPS task CVEL. For all fields, self-calibration was carried out to mitigate the effects of side lobes from strong continuum sources, with side lobes from 3C264 presenting a particular problem. Self–calibration improved on the standard complex gain calibration and in all cases the solutions converged on the first iteration (phase only). Our final data cubes were produced with robust weighting (ROBUST = 0) and have a spatial resolution of ∼15 arcsec. The ROBUST option corrects the weights of the visibilities in the Fourier transform for the fact that there is a much higher density of measured visibilities in the inner part of the *uv*-plane compared to the outer regions (Briggs 1995). This comes at a cost of a slightly increased noise compared to using what is known as 'natural weights'. Natural weighting leads to a conversion to brightness temperature, $T_{\rm B}$, of 1 mJy beam^{-1} = 3 K. Appendix B gives further details of the observational set up for the individual VLA fields.

It was found that continuum subtraction was a critical step in the data reduction. Ordinarily, one would search for line-free channels in each cube and then use, e.g. UVLIN to subtract the continuum. The problem with our observations was that in several cubes some H I emission was detected in almost every channel. This required a more elaborate approach consisting of deriving a continuum map made up of the average of line-free channels at each spatial position in the cube. This map was subsequently subtracted from the line + continuum data to produce cubes containing only line emission. In practice, this required the following procedure. First, emission from continuum sources with flux density greater than the estimated peak H I emission, normally ∼5 mJy beam^{-1}, was modelled and removed in the *uv*-plane with AIPS task UVSUB. This resulted in cubes containing *line + residual continuum* sources. In the second stage, AIPS tasks BLANK and SQASH were used to create an image of the average residual continuum in the line-free channels at each spatial position by masking regions of the cube clearly containing H I emission. The average continuum image was subtracted from the line plus residual continuum cube, producing a cube which more clearly delineated the extent of H I emission. In the third stage, the previous cube was smoothed with AIPS tasks CONVL and a second average continuum image was made but this time masking the H I from cube produced in the previous stage. This second version of the residual continuum map was then subtracted from original *line + residual continuum* data to produce the final cubes containing only line emission and much reduced rms noise compared to using UVLIN OR UVLSF. Table 1 shows the approximate rms per channel for the final cubes. For consistency, we applied the above continuum subtraction method to all of the cubes.

3 VLA C-ARRAY RESULTS

Velocity integrated H I maps and velocity fields for each of the 15 H I detections from our C-array observations and CGCG 097−062 from NRAO VLA archival data (16 VLA C-array detections in total) are presented in Appendix A. A brief analysis for each C-array detection is also included in Appendix A. Basic properties for each of the 16 C-array detections, including CGCG 097−062, are given in Table 2 with a summary of their H I properties given in Table 3. The column labelled 'Flux VLA/AGES' in Table 3 gives the fraction of H I flux recovered by the C-array observations in comparison to that from the AGES Arecibo single-dish H I survey (Cortese et al. 2008). For all but three galaxies the C-array recovered >70 per cent of the AGES H I flux. The two poorest C-array flux recoveries were for CGCG 097−087 (0.47) and the CGCG 097−102 pair (0.60).

Table 1. VLA C-array observational parameters.

Field[a]	Day[b]	IF	α_{2000} (^{h} ^{m} ^{s})	δ_{2000} ($^\circ$ $'$ $''$)	Int. time (h)	Beam[c] size ($''$)	Central velocity (km s^{-1})	Rms noise per channel (mJy)	Detection NH I[d] limit $\times 10^{19}$ (atoms cm^{-2})	Detection[e] limit $\times 10^7$ (M$_\odot$)
B	5	1	11 44 50.0	19 47 00	9.3	21 × 18	8200	0.28	1.8	5.5
B	5	2	11 44 50.0	19 47 00	9.3	21 × 18	5100	0.29	1.9	5.7
C	1	1	11 42 30.4	20 07 41	16.7	19 × 18	5800	0.22	1.6	4.4
C	1	2	11 42 30.4	20 07 41	16.7	19 × 18	6300	0.22	1.6	4.4
C	2	1	11 42 30.4	20 07 41	2.0	20 × 18	7100	0.70	4.7	13.9
C	2	2	11 42 30.4	20 07 41	2.0	20 × 18	7600	0.70	4.7	13.9
D	3	1	11 44 45.6	20 05 24	8.9	14 × 15	7400	0.34	3.9	6.7
D	3	2	11 44 45.6	20 05 24	8.9	14 × 15	5100	0.35	4.0	6.9
D	4	1	11 44 45.6	20 05 24	9.3	14 × 15	6500	0.25	2.9	5.0
D	4	2	11 44 45.6	20 05 24	9.5	14 × 15	7000	0.25	2.9	5.0

Notes. [a]VLA Project ID: AB1285.
[b]Details of each day's observations are given in Appendix B.
[c]For robust 0 cubes.
[d]3σ in two consecutive channels of 11 km s^{-1} each.
[e]3σ in two consecutive channels of 11 km s^{-1} each, with distance = 92 Mpc.

Table 2. VLA C-array detections H I: basic properties.

Galaxy ID[a]	RA (^{h} ^{m} ^{s})	Dec. ($^\circ$ $'$ $''$)	V_{opt}[b] (km s^{-1})	Hubble[c] type	Major axis[d] (arcmin)
CGCG 097−125	11 44 54.8	+19 46 35	8225	Sa	0.92
[SKV2002]K2	11 44 50.6	+19 46 02	8152	H II	–
CGCG 097−114	11 44 47.8	+19 46 24	8293	Pec	0.48
CGCG 097−129W	11 45 03.9	+19 58 25	5091	Sb	2.77
CGCG 097−138	11 45 44.7	+20 01 52	5322	Pec	0.65
CGCG 097−068	11 42 24.5	+20 07 09	5974	Sbc	1.14
J114229.18+200713.7	11 42 29.2	+20 07 14	6250	Irr	–
CGCG 097−062	11 42 14.8	+19 58 36	7815	Pec	0.86
CGCG 097−063	11 42 15.6	+20 02 56	6087	Pec	0.58
CGCG 097−072	11 42 45.1	+20 01 56	6338	Sa	1.11
CGCG 127032	11 42 09.1	+20 18 56	5764	S0	1.47
CGCG 097−087	11 43 49.1	+19 58 06	6725	Pec	1.86
CGCG 097−121	11 44 47.0	+20 07 30	6583	Sab	1.25
CGCG 097−97102N	11 44 17.2	+20 13 24	6368	Sa	1.04
CGCG 097−091	11 43 58.9	+20 04 37	7372	Sa	1.15
J114250.97+202631.8	11 42 51.0	+20 26 32	5718	S	0.70

Notes. [a]CGCG IDs are from the Zwicky catalogue of Galaxies and Cluster Galaxies (Zwicky, Herzog & Wild 1968, CGCG). IDs with the prefix J are from SDSS, J114229.18+200713.7 = SDSS J114229.18+200713.7 and J114250.97+202631.8 = SDSS J114250.97+202631.8. K2 refers to the extragalactic H II region [SKV2002]K2 in the BIG compact group (Cortese et al. 2006).
[b]V_{opt} = optical velocity from NED.
[c]From NED, except [SKV2002]K2 which is from Cortese et al. (2006).
[d]Major axis diameters are r-band (SDSS Isophotal) diameters from NED, except for CGCG 097−072, CGCG 127032 which are K_s (2MASS 'total') diameters from NED and CGCG 097−138, CGCG 097−087 which are 25 mag arcsec^{-2} isophotal B-band level diameters from Hyperleda.

For CGCG 097−087, our previous VLA D-array observations (Paper I) recovered almost 100 per cent of the AGES H I flux and revealed an extensive low surface brightness region NW of the optical disc. Comparing the VLA C- and D-array maps as well as the AGES spectrum reveals the bulk of missing C-array flux is higher velocity H I located NW of the optical centre, and in particular in its ~70 kpc H I tail reported in Paper I. The 95 per cent C-array H I flux recovery for our largest H I diameter (~3 arcmin, 75 kpc) spiral, CGCG 097−129W, lead us to rule out lack short spacings as the reason for the missing C-array flux. We therefore conclude that the interaction CGCG 097−087 is undergoing has produced extensive regions of low surface brightness H I which are below the C-array detection threshold of 2.9×10^{19} cm^{-2}, but above the D-array detection threshold of 1.9×10^{19} cm^{-2}. The H I morphology and velocity field for CGCG 097−087 (Fig. A7) supports the ram pressure plus tidal interaction with CGCG 097−087N scenario proposed in Consolandi et al. (2017), see Appendix A. In the case of the CGCG 097−102 pair, the C-array H I morphology and kinematics as well as NIR asymmetry analysis provide evidence indicative of a recent tidal interaction (see Appendix A). As in CGCG 097−087, undetected low-density H I debris from the interaction could possibly account for the missing C-array flux in the CGCG 097−102 pair.

The H I morphologies and/or kinematics of almost all of the 15 LTGs presented in Appendix A show significant signatures of a recent or ongoing perturbation, e.g. CGCG 097−121 (Fig. A11)

Table 3. H I properties for the VLA C-array H I detections.

Galaxy ID[a]	$V_{H I}$[b] VLA–C (km s^{-1})	W_{20}[c] VLA–C (km s^{-1})	H I offsets VLA–C $> 2\sigma$ (arcsec)	H I offsets AGES $> 2\sigma$ (arcsec)	A_{flux}[d] AGES	Flux[e] VLA/AGES (fraction)	M(H I)[f] AGES (10^9 M$_\odot$)	Def. H I[g] AGES	Sub[h] cluster distance (kpc)
CGCG 97−125	8277 ± 18	424 ± 36	14.4 ± 2.9	–	1.47 ± 0.09				121
[*SKV*2002] K2	8152 ± 10	261 ± 19	–	–	1.19 ± 0.04	} 1.27	} 4.7	} 0.1	101
CGCG 97−114	8451 ± 20	54 ± 40	10.4 ± 2.9	–	1.13 ± 0.07				109
CGCG 97−129W	5102 ± 11	512 ± 22	13.1 ± 2.9	–	1.19 ± 0.02	0.95	7.8	− 0.1	362
CGCG 97−138	5315 ± 2	64 ± 3	8.1 ± 3.3	–	1.17 ± 0.03	0.65	2.0	− 0.1	610
CGCG 97−068	5969 ± 11	355 ± 21	18.6 ± 2.9	–	1.12 ± 0.01	} 1.12	} 7.2	} − 0.3	621
J114229.18+200713.7	6114 ± 2	86 ± 5	7.9 ± 2.9	–	1.52 ± 0.02				597
CGCG 97−062	7803 ± 12	228 ± 25	–	39.6 ± 15.2	1.90 ± 0.04	0.96	2.5	0.3	626
CGCG 97−063	6082 ± 2	172 ± 3	–	–	1.22 ± 0.08	0.87	1.3	0.0	637
CGCG 97−072	6327 ± 21	301 ± 41	8.6 ± 2.9	–	1.03 ± 0.05	1.09	0.9	0.5	464
CGCG 127−032	5738 ± 11	311 ± 21	30.8 ± 2.9	29.5 ± 14.5	1.13 ± 0.02	0.73	1.9	0.3	853
CGCG 97−087	6729 ± 11	561 ± 22	10.9 ± 2.9	–	1.82 ± 0.09	0.47	5.9	0.4	80
CGCG 97−121	6578 ± 63	388 ± 126	13.6 ± 2.9	–	1.92 ± 0.08	1.09	1.3	0.4	370
CGCG 97−102N	6373 ± 11	302 ± 22	11.1 ± 2.9	–	1.22 ± 0.07	0.60	1.0	0.4	411
CGCG 97−091	7372 ± 2	260 ± 4	9.0 ± 2.9	–	1.17 ± 0.02	0.87	6.5	− 0.2	190
J114250.97+202631.8	5705 ± 3	130 ± 6	10.6 ± 2.9	N/A	1.17 ± 0.07	N/A	2.7	− 0.5	841

[a]See Table 2 note a.

[b]$V_{H I}$ calculated using the method described in Paper I.

[c]W_{20} calculated using the method described in Paper I.

[d]AGES A_{flux} as defined in Section 5.1. In two cases, (CGCG 097−125, K2, CGCG 097−114) and (CGCG 097−068, SDSS J114229.18+200713.7), VLA H I detections are confused within the 3.5 arcmin AGES FWHP beam and in these cases the A_{flux} in the table was measured from the VLA C-array spectra rather than the AGES spectra.

[e]As noted in footnote d, some H I detections are confused in the AGES FWHP beam. In those cases, the brackets in the table indicate the discrete VLA H I detections which are included in each integrated AGES Flux value and similarly for the AGES M(H I) and the H I deficiency values.

[f]Based on the flux from AGES, except for SDSS J114250.97+202631.8 and cases were the galaxy is confused in the AGES FWHP beam, i.e. for CGCG 097−125, [*SKV*2002]*K*2, CGCG 097−114, CGCG 097−068, SDSS J114229.18+200713.7 which are from their VLA C–array spectra. $M(H I) = 2.36 \times 10^2$ D^2 $S_{H I}$ where $M(H I)$ is in M$_\odot$, D = distance (92 Mpc) and $S_{H I}$ is the AGES or VLA flux in mJy.

[g]H I deficiencies are calculated using the method as described in Paper I.

[h]Projected distance from the nearest A1367 subcluster ICM core assuming a spatial scale at the cluster distance of 24.8 kpc per arcmin. For CGCG 097−114, CGCG 097−125, and [*SKV*2002]*K*2 the nearest subcluster in projection is the SE subcluster and in all other cases it is the NW subcluster.

which could be an example of ongoing ram-pressure stripping; CGCG 097−068 (Fig. A4) has a morphology and kinematics which could be explained by a ram pressure and/or a tidal interaction. CGCG 097−062 (Fig. A2) displays a cometary morphology at both optical and H I wavelengths.

We tried to fit rotation curves to H I emission in the A1367 C-array cubes using ^{3D}BAROLO software (Di Teodoro & Fraternali 2015). Despite experimenting with different parameters, including binning the cube along the velocity axis, the ^{3D}BAROLO fits either failed or were too poor to be useful. This appeared to be the result of an unfortunate combination of the low number of beams across the galaxies (typically 3 or 2), low signal-to-noise ratio (S/N) and in almost all cases evidence from the integrated maps that the H I discs are significantly perturbed.

4 A1367: CUMULATIVE H I DATA

The A1367 field within the AGES single-dish blind H I survey, carried out with the 305-m Arecibo telescope using the ALFA[13] receiver, covers a ∼5° × 1° sky area centred on the core of A1367. At A1367's distance, the AGES survey covers a projected area of ∼7.4 Mpc^2 and extends in RA, east and west, beyond the A1367 virial radius (see Fig. 2). H I detections in the AGES A1367 field

---

[13] The seven-beam Arecibo L-Band Feed Array (ALFA) receiver (Giovanelli et al. 2005).

were made in the velocity range 1142–19 052 km s^{-1}. Full details of the AGES survey are given in Cortese et al. (2008). For this study, we define the 5° × 1° sky area of the AGES A1367 field with a more restricted velocity range of 4600–8600 km s^{-1} as the 'A1367 volume'. This more restricted velocity range is approximately 4 times the 891 ± 58 km s^{-1} velocity dispersion of the cluster (Cortese et al. 2004). Our study uses the AGES third data release positions in the A1367 volume as the projected positions of the AGES H I. Within the A1367 volume, there are 47 AGES H I detections with optical counterparts. Five of these have severe radio frequency interference (RFI) features in their spectra making their H I positions and spectra unreliable. For one of these galaxies (CGCG 097−079), the position and spectrum from the low-resolution VLA D-array map was substituted for the AGES data. For CGCG 097−079, the integrated H I flux from VLA D-array observations was 0.518 Jy km s^{-1} compared to 0.247 Jy km s^{-1} from AGES, which reflects the impact of RFI on the AGES spectrum. We excluded the other four galaxies from our analysis. For the remaining 43 AGES detections, the mean AGES H I positional uncertainties are RA: (11.72 ± 3.21 arcsec) and Dec. (11.23 ± 2.37 arcsec). We were concerned the AGES positions might be affected by systematic pointing errors. In that case, errors in RA would be expected to dominate over Dec. errors because of the drift scanning observation method used at Arecibo. Our tests found no indication that the AGES offsets or their position angles (PA) are correlated with either RA or Dec.

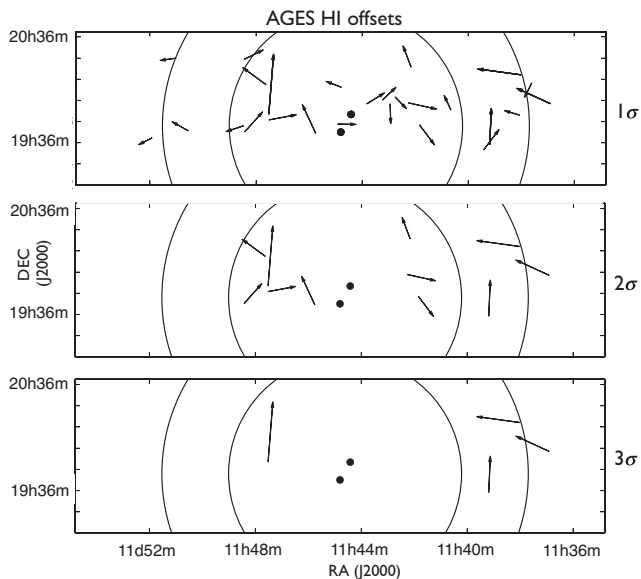Within the A1367 volume, there are 29 LTGs and an extragalactic H II region (30 objects) with VLA C-array and/or D-array resolved

Figure 2. Projected AGES H I offsets within the ~1° × 5° 4600–8600 km s⁻¹ A1367 volume. The arrows indicate the magnitude (×20) and direction (from the galaxy optical centre) of the H I offsets. The top, middle, and bottom panels show the AGES H I offsets $>1\sigma$, $> 2 >$, and $>3\sigma$ pointing uncertainties, respectively. The centres of the A1367 SE and NW subclusters are indicated with filled circles. The smaller of the two large circles indicates the ~1.64 Mpc (1°.1) A1367 R_{200} radius with the larger circle showing the virial radius ~2.57 Mpc (1°.73).

H I maps with optical counterparts (Papers I, II, and this paper). The position of the H I column density maximum in each object was determined from the maps. Positional uncertainties for the H I column density maxima in the maps are ~2 and ~4 arcsec for the VLA C and D arrays, respectively. For 21 LTGs in the A1367 volume, we have both VLA H I column density maxima positions and AGES H I positions. Nine VLA H I detections are not in AGES and are, with one exception, galaxies resolved in the VLA maps but confused within the larger ~3.5 arcmin Arecibo FWHP beam. The exception is SDSS J114250.97+202631.8 which was mapped with the VLA C array but was not reported in AGES because it was only partially detected at the northern edge of the AGES field.

5 DISCUSSION

We investigated the resolved VLA and unresolved AGES H I data within the A1367 volume with the aim of understanding the magnitude and spatial distribution of LTG H I perturbation signatures. This involved analysis of four quantifiable H I perturbation signatures: (i) the asymmetry between the upper and lower wings of the H I profile; (ii) the difference between the optical and H I velocities; (iii) the projected offset between AGES H I position and the centre of its optical counterpart (AGES H I offset); (iv) the offset between the position of the H I column density maximum in a galaxy's resolved VLA map and the centre of its optical counterpart (VLA H I offset). Calculations of these offsets used the optical positions from NED, or if unavailable from SDSS. We assume that the optical positions trace the deepest part of the galaxies' potentials. The optical positions typically have uncertainties of 0.5 arcsec or less. Table 4 gives the AGES H I offset, and where available the VLA H I offset, for the 43 H I AGES detections with optical counterparts in the A1367 volume. The table also gives the H I spectral asymmetry ratios (A_{flux}) from the AGES spectra and the offset between the AGES H I and op-

tical velocities. We considered the relation of these H I perturbation signatures to selected properties of their galaxies and the cluster. Additionally to assess the frequency and strength of H I perturbations in A1367 relative to other nearby clusters, we determined the A_{flux} distribution for a sample of Virgo cluster galaxies.

5.1 H I spectral profiles – A_{flux}

A galaxy's A_{flux} ratio is a measure of the asymmetry in its integrated H I flux density profile (within its W_{20} velocity range) at velocities above and below the galaxy's systemic velocity, $V_{\text{H I}}$, see Espada et al. (2011) including graphical examples in their figs 3 and 4. Even isolated LTGs display a scatter of A_{flux} ratio, which is well characterized by a half Gaussian, with its mean equal to 1.0 and a 1σ dispersion of 0.13. This half Gaussian was obtained from a fit to the distribution of A_{flux} values from a sample of AMIGA[14] isolated galaxies (Espada et al. 2011). The value of an A_{flux} deviating by 1σ from the mean of that distribution is then 1.13. In Fig. 3 (upper panel), we show a histogram of the distribution of AGES A_{flux} ratios for the 43 A1367 AGES H I detected LTGs compared to the half Gaussian fit for A_{flux} ratios from the AMIGA sample of isolated galaxies: 11 (26 per cent) of the 43 LTGs have an AGES A_{flux} ratio greater than 1.39, the 3σ value from the AMIGA sample. The penultimate column of Table 4 shows the A_{flux} values for the A1367 LTGs and those with $A_{\text{flux}} > 1.39$ are highlighted in bold typeface. The 26 per cent for A 1367 is significantly greater than the 2 per cent for the AMIGA sample and above the 10 per cent–20 per cent which Espada et al. (2011) reported for other samples from environments with higher galaxy densities. Assuming the 2 per cent of galaxies with $A_{\text{flux}} > 3\sigma$ ($A_{\text{flux}} = 1.39$) from the AMIGA study reflects the intrinsic A_{flux} variation in a galaxy population. It then follows that the presence of a larger fraction of galaxies with $A_{\text{flux}} > 1.39$ in samples from higher galaxy density environments can be attributed to perturbations caused by interactions with the environment. In the field, pair or group tidal interactions are probably responsible, whereas in clusters both tidal and ram-pressure interactions are the probable sources of the H I perturbations.

Ideally, we would search for statistically significant correlations between $A_{\text{flux}} > 3\sigma$ and other LTG properties, but the small number of LTGs matching this criterion makes this impractical. However, there are 17 LTGs with AGES A_{flux} greater than the 2σ AMIGA value of 1.26 (AGES $A_{\text{flux}} > 2\sigma$ from now on) and for these LTGs we carried out tests for statistically significant correlations between their A_{flux} and their: AGES H I offsets, subcluster distance, H I deficiency, H I mass, SDSS $g - i$ colour, optical disc inclination, and mean S/N in the AGES spectrum. Table 5 sets out the Pearson and Spearman r- and p-values from these tests. We emphasize the tests are only for LTGs with $A_{\text{flux}} > 2\sigma$. For the relations between AGES $A_{\text{flux}} > 2\sigma$ versus subcluster distance and AGES $A_{\text{flux}} > 2\sigma$ versus H I deficiency, the null hypothesis that the variables are uncorrelated is rejected by a one-tail directional test with 99 per cent and 97.5 per cent confidence, respectively. However, while statistically significant these correlations are rather weak and are not found if the sample is restricted to members with $A_{\text{flux}} > 3\sigma$. In all other cases, the null hypothesis of no correlation is accepted with 99 per cent confidence level. Fig. 4 shows plots of both of these relations with a linear fit added for galaxies with an AGES A_{flux} ratio $> 2\sigma$ (a fit exclusively to the black symbols above the dashed lines in the figures). Fig. 4 (left) shows a trend for the AGES A_{flux} ratio $> 2\sigma$ to

[14] Analysis of the interstellar Medium of Isolated GAlaxies.

Table 4. A 1367: magnitude of resolved and unresolved H I offsets, A_{flux}, and H I/optical velocity difference.[a]

Optical ID[b] Source	RA AGES	Dec. AGES	H I offset[c] AGES	H I offset AGES	H I offset[d] AGES angle	H I offset VLA	A_{flux}[e] AGES	ΔV[f] AGES – optical
	(^{h} ^{m} ^{s})	($^\circ$ $'$ $''$)	(arcsec)	(kpc)	($^\circ$)	(arcsec)		(km s^{-1})
SDSS J113544.31+195114.0	11 35 45.3	19 51 20	16 ± 16.3	7 ± 7	68.0	–	**1.71 ± 0.06**	0.0 ± 9.9
CGCG 097−027	11 36 54.2	20 00 03	13 ± 15.2	5 ± 6	357.6	17.9 ± 5.7	1.04 ± 0.07	0.0 ± 8.5
CGCG 097−026	11 36 57.6	19 58 37	**52.8 ± 14.5**	**22 ± 6**	**65.4**	8.3 ± 5.7	1.3 ± 0.08	0.0 ± 4.2
CGCG 097−033	11 37 36.5	20 09 34	18.3 ± 15.2	8 ± 6	153.2	–	1.02 ± 0.04	0.0 ± 4.2
AGC 210538	11 38 05.0	19 51 46	17.2 ± 14.6	7 ± 6	73.1	7.6 ± 5.9	1.04 ± 0.04	0.0 ± 4.2
ASK 627362.0	11 38 05.0	20 14 41	**64.6 ± 18.6**	**27 ± 8**	**82.3**	–	**1.46 ± 0.11**	0.0 ± 5.7
CGCG 097−036	11 38 51.3	19 36 22	17.4 ± 34.2	7 ± 14	15.7	8.6 ± 5.7	**1.44 ± 0.05**	0.0 ± 8.5
FGC 1287	11 39 10.8	19 35 58	**52.0 ± 14.6**	**22 ± 6**	**357.5**	9.6 ± 5.9	1.38 ± 0.06	**42.0 ± 7.1**
CGCG 097−041	11 39 23.1	19 32 32	**33.9 ± 17.7**	**14 ± 7**	**322.9**	3.6 ± 5.7	1.02 ± 0.02	**5.0 ± 3.6**
ASK 629113.0	11 40 39.5	19 54 55	18.1 ± 15.2	7 ± 6	24.8	–	1.06 ± 0.06	0.0 ± 4.2
ABELL 1367:[GP82] 1512	11 41 48.5	19 45 38	**33.1 ± 14.5**	**14 ± 6**	**217.0**	–	1.18 ± 0.07	0.0 ± 8.5
CGCG 127−032	11 42 09.8	20 19 24	**29.5 ± 14.5**	**12 ± 6**	**20.7**	30.8 ± 2.9	1.13 ± 0.02	0.0 ± 7.1
CGCG 097−062	11 42 12.2	19 58 27	**39.6 ± 15.2**	**16 ± 6**	**257.6**	4.1 ± 2.9	**1.90 ± 0.04**	**41.0 ± 6.7**
CGCG 097−063	11 42 16.5	20 03 02	14.2 ± 29.5	6 ± 12	62.9	2.3 ± 2.9	1.22 ± 0.08	0.0 ± 7.1
CGCG 097−068	11 42 24.9	20 07 10	6.1 ± 14.5	3 ± 6	85.2	18.6 ± 2.9	1.12 ± 0.01	**5.0 ± 2.8**
CGCG 097−072	11 42 44.3	20 01 43	18.6 ± 15.2	8 ± 6	224.2	8.6 ± 2.9	1.03 ± 0.05	0.0 ± 4.2
CGCG 097−073	11 42 56.4	19 57 34	24.4 ± 14.5	10 ± 6	181.9	4.4 ± 5.7	1.14 ± 0.06	**11.0 ± 9.2**
CGCG 097−079	11 43 12.3	20 00 32	22.3 ± 15.3	9 ± 6	313.7	13.8 ± 3.2	**2.06 ± 0.08**	0.0 ± 9.9
ABELL 1367:[GP82] 1227	11 43 12.5	19 36 55	11.8 ± 14.9	5 ± 6	313.6	5.6 ± 6.7	1.04 ± 0.05	8.0 ± 11.7
CGCG 097−087	11 43 47.6	19 58 20	25.9 ± 14.5	11 ± 6	301.7	10.9 ± 2.9	**1.82 ± 0.09**	**179.0 ± 8.2**
CGCG 097−091	11 43 59.0	20 04 30	7.3 ± 14.5	3 ± 6	175.4	9 ± 2.9	1.17 ± 0.02	0.0 ± 2.8
CGCG 097−102N	11 44 16.9	20 13 09	15.6 ± 17	6 ± 7	197.5	11.1 ± 2.9	**1.46 ± 0.02**	2.0 ± 15.2
CGCG 097−121	11 44 48.2	20 07 37	18.6 ± 15.2	8 ± 6	69.1	13.6 ± 2.9	**1.92 ± 0.08**	0.0 ± 4.2
CGCG 097−122	11 44 52.3	19 27 23	7.9 ± 14.5	3 ± 6	6.5	–	1.23 ± 0.03	10.0 ± 10
CGCG 097−125	11 44 53.4	19 46 35	21.8 ± 14.5	9 ± 6	269.2	14.4 ± 2.9	**1.47 ± 0.09**	0.0 ± 11.3
CGCG 097−129W	11 45 03.7	19 58 32	7.3 ± 14.5	3 ± 6	337.8	13.1 ± 2.9	1.19 ± 0.02	0.0 ± 2.8
CGCG 097−138	11 45 44.0	20 01 47	11.1 ± 14.6	5 ± 6	245.4	8.1 ± 3.3	1.17 ± 0.03	0.0 ± 2.8
ABELL 1367:[GP82] 0328	11 45 46.4	19 42 10	**44.3 ± 17.3**	**18 ± 7**	**24.9**	–	1.25 ± 0.07	0.0 ± 9.9
SDSS J114725.07+192331.3	11 47 24.6	19 23 24	10.3 ± 14.5	4 ± 6	224.3	–	1.09 ± 0.02	0.0 ± 5.7
SDSS J114730.39+194859.0	11 47 27.9	19 49 06	**38 ± 16.3**	**16 ± 7**	**280.6**	–	1.06 ± 0.05	0.0 ± 9.9
ABELL 1367:[BO85] 092	11 47 30.5	19 53 53	**92.7 ± 18.5**	**38 ± 8**	**355.4**	–	1.09 ± 0.04	19.0 ± 28.4
CGCG 097−152	11 47 40.2	19 56 21	12.8 ± 14.5	5 ± 6	93.3	–	1.12 ± 0.04	0.0 ± 2.8
SDSS J114737.56+200900.5	11 47 39.7	20 09 24	**39.6 ± 14.5**	**16 ± 6**	**53.8**	–	1.19 ± 0.03	0.0 ± 7.1
SDSS J114825.21+194217.0	11 48 23.6	19 42 44	**36.2 ± 14.5**	**15 ± 6**	**318.2**	–	**1.69 ± 0.03**	0.0 ± 9.9
LSBC D571-02	11 48 24.8	20 23 31	26.9 ± 22	11 ± 9	296.4	–	**1.45 ± 0.07**	0.0 ± 11.3
MAPS-NGP O-434-31444	11 48 29.8	19 45 29	22 ± 20.1	9 ± 8	108.4	–	1.29 ± 0.04	0.0 ± 5.7
MAPS-NGP O-434-21239	11 50 30.5	20 05 05	8.6 ± 16.7	4 ± 7	109.7	–	1.10 ± 0.06	0.0 ± 9.9
SDSS J115033.61+194250.1	11 50 34.9	19 43 01	22.2 ± 14.5	9 ± 6	60.7	–	1.31 ± 0.05	0.0 ± 9.9
CGCG 127−072	11 51 02.3	20 23 55	18.1 ± 14.5	7 ± 6	98.2	–	1.04 ± 0.03	0.0 ± 2.8
KUG 1149+199	11 51 56.6	19 38 38	16.1 ± 14.5	7 ± 6	117.2	–	1.2 ± 0.02	0.0 ± 2.8
KUG 1149+206	11 52 24.0	20 19 43	15.6 ± 16.0	6 ± 7	335.1	–	1.06 ± 0.04	0.0 ± 7.1
KUG 1150+203	11 53 18.5	20 06 22	7 ± 14.9	3 ± 6	141.8	–	1.37 ± 0.04	0.0 ± 4.2
CGCG 097−180	11 54 14.6	20 01 38	9.9 ± 15.3	4 ± 6	95.8	–	1.35 ± 0.06	0.0 ± 4.2

Notes. [a]VLA H I detections CGCG 097−114 and J114229.18+200713.7 in Table 3 were excluded from this table because they are confused in the AGES FWHP beam with LTGs with much larger H I masses, which prevented reliable AGES spectra being extracted for them. J114250.97+202631.8, although detected with the VLA, was excluded from this table because it does not have an AGES spectrum (see Section 4.)
[b]See Table 3 note a.
[c]Projected offsets between the AGES H I and optical positions. Offset uncertainties were calculated in quadrature using both the AGES H I and NED optical velocity uncertainties. Offsets $>2\sigma$ are highlighted with bold typeface.
[d]Offset angles are the counter clockwise angle in degrees from the north, with the origin at the optical position, for a vector joining the optical and AGES H I positions. LTGs with AGES H I position offsets $>2\sigma$ are highlighted with bold typeface.
[e]For CGCG 097−068 and CGCG 097−125 the A_{flux} is from the VLA C-array spectra, see Table 3 footnote d. LTGs with $A_{flux} > 1.39$ are shown in bold typeface.
[f]Difference between the AGES H I and optical velocity. Velocity differences greater than their 3σ velocity uncertainties are highlighted with bold typeface, with the uncertainties calculated in quadrature using both the AGES H I and NED optical velocity uncertainties.

increase towards the cluster centre, although this is characterized by significantly larger A_{flux} ratios near the subcluster cores with smaller ratios at radial distances >1.5 Mpc. The round open symbols in the Fig. 4 represent members of pairs or groups (close companions per NED): 5 out of 9 (56 per cent) these pair or group members have A_{flux} ratios $> 2\sigma$ and make up 31 per cent of the galaxies with A_{flux} ratios $> 2\sigma$. We used NED to define a search volume, using a search radius of 26 arcmin (750 kpc) and $\pm$ 1000 km s^{-1}, creating
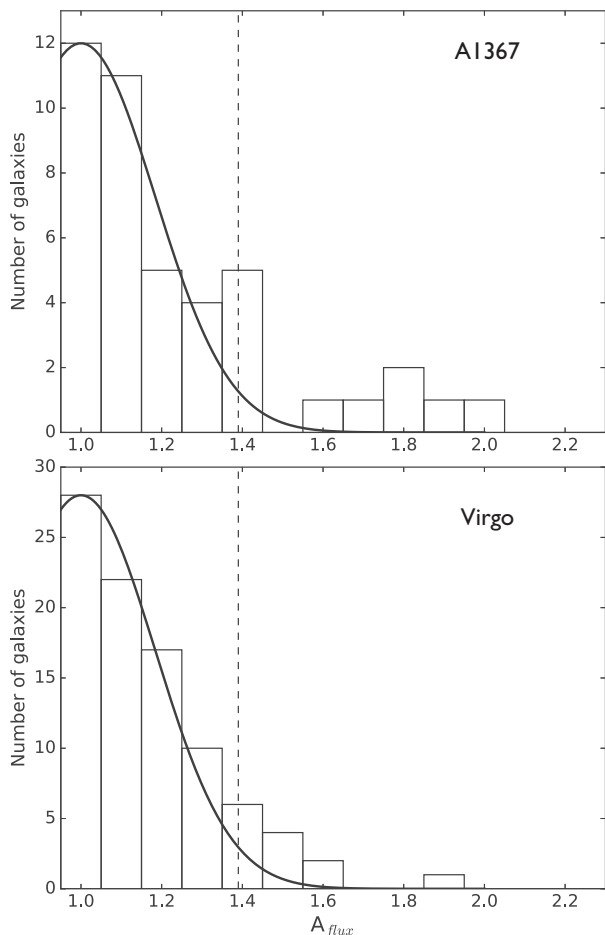
Figure 3. Distribution of A_{flux} ratios in A1367 and Virgo compared to the half Gaussian fit to the A_{flux} distribution from the AMIGA sample of isolated galaxies. Top: histogram of A_{flux} for LTGs within the A1367 volume. Bottom: histogram of A_{flux} for galaxies within the Virgo–ALFALFA volume. The Virgo sample includes only galaxies with $M(H I) > 3 \times 10^8$ $M_\odot$, i.e. the lowest H I mass LTG in our A1367–AGES sample. The half Gaussian fit maximum has been scaled to the highest value histogram bin. The dashed line indicates the 3σ value (1.39) from the half Gaussian fit to the distribution of A_{flux} in a sample of AMIGA isolated galaxies.

a (fairly) complete list of all companions for each LTG, late- as well as early-type galaxies. One of our LTGs was deemed to be in a pair or group if a cluster galaxy was present within a projected separation of 5 arcmin (145 kpc) and radial velocity separation of less than $\pm 300\,\mathrm{km\,s^{-1}}$ (except for the two principal members of the RSCG 42 which have a velocity separation of $447\,\mathrm{km\,s^{-1}}$). The correlation between A_{flux} ratio $> 2\sigma$ and H I deficiency indicates an elevated A_{flux} ratio is associated with ongoing or recent stripping of H I from cluster LTGs. We note that both statistically significant relations are observed despite the self-evident exclusion of LTGs without H I detections, referred to in Paper I, which were presumably previously stripped of their H I.

Our tests (Table 5) did not find a statistically significant correlation between AGES $A_{flux} > 2\,\sigma$ and AGES H I offsets $> 2\sigma$. However, all galaxies with resolved one-sided H I tail morphologies also have $A_{flux} > 2\sigma$ and the magnitude of their AGES H I offsets are larger than their VLA H I offsets (Fig. 5), consistent with the single-dish observations being sensitive to displaced low-density H I. Moreover, there are five cases (CGCG 097−026, ASK 627362.0, FGC 1287, CGCG 097−062, and SDSS J114825.21+194217.0)

where both the AGES H I offset and A_{flux} interaction signatures $> 2\sigma$ are present. For three of them we have VLA H I maps showing morphology and kinematics consistent with strongly perturbed H I. Overall we conclude A_{flux} can be a useful indicator of ongoing and/or recent H I perturbation and the large fraction of A 1367 LTGs with $A_{flux} > 1.39$ adds to the evidence that such perturbations are strong and widespread in A1367.

5.2 H I/optical – velocity offsets

For the AGES-detected LTGs (excluding those with RFI contamination), we compared their AGES H I and optical velocities. Six LTGs had velocity differences greater than their 3σ velocity uncertainties, with the uncertainties calculated in quadrature using both the AGES H I and NED optical velocity uncertainties. Those LTGs and the their velocity differences are highlighted with bold typeface in the final column of Table 4. It is notable that the three LTGs with a velocity difference $> 40\,\mathrm{km\,s^{-1}}$ (FGC 1287, CGCG 097−062, and CGCG 097−087) all have clearly discernible H I tails in resolved maps and optical disc inclinations $\geq 69°$.

5.3 H I optical – spatial offsets

5.3.1 Unresolved AGES H I offsets

Table 6 summarizes the number of AGES H I offsets $> 1\sigma$, $> 2\sigma$, and $> 3\sigma$ pointing uncertainties. The AGES H I offset uncertainties were determined in quadrature using the NED optical and H I AGES positional uncertainties. 11 (26 per cent) of the 43 AGES detections with optical counterparts in the A1367 volume have AGES H I offsets $> 2\sigma$ pointing uncertainties (referred to as AGES H I offsets $> 2\sigma$ from now on) and they are highlighted with bold typeface in the columns headed H I offsets AGES in Table 4. Fig. 2 shows the magnitudes (scaled $\times 20$) of the AGES H I offsets $> 1\sigma$, $> 2\sigma$, and $> 3\sigma$ with arrowheads indicating the projected direction of each offset from the galaxy's optical centre to its AGES H I position. We note from Fig. 2 that the largest magnitude offsets are not preferentially found near the subcluster cores, with three of the four AGES H I offsets $> 3\sigma$ projected beyond the R_{200} radius. Two of these offsets (CGCG 097−026 and FGC 1287) are known from VLA H I mapping to contain long ∼160 and ∼250 kpc H I tails, respectively (Paper II).

We carried out tests for statistically significant correlations between the AGES H I offsets $> 2\sigma$ and subcluster distance, H I deficiency, H I mass, SDSS $g - i$ colour, optical disc inclination, and mean S/N in the AGES spectrum. Based on the Pearson correlation coefficient, $r(\mathrm{df}^{15} = 9)$, and a one-tailed test, the null hypothesis that each of these variables are uncorrelated to AGES H I offsets $> 2\sigma$ is accepted with a 99.95 per cent confidence level. Table 5 sets out the r- and p-values from these tests.

5.3.2 Resolved VLA H I offsets

12 LTGs (40 per cent) of the 30 objects with resolved VLA H I offsets show VLA H I offsets greater than the 2σ VLA/optical pointing uncertainties. To determine whether the magnitude of the A1367 resolved VLA H I offsets were abnormally large, we compared them with the resolved H I offsets from 32 high-resolution VLA H I

---

[15] Degrees of freedom = sample size − 2.

Table 5. AGES $A_{flux} > 2\sigma$ and AGES H I offset $> 2\sigma$ relations, r- and p-values.

	Pearson		Spearman	
Relation	r-value[a]	p-value	r_s	p-value
$A_{flux} > 2\sigma$				
AGES H I offset	−0.063	0.810	0.071	0.786
Subcluster distance	**−0.598**	**0.011**	−0.646	0.005
H Ideficiency	**0.522**	**0.031**	0.658	0.004
H I mass	−0.240	0.353	−0.210	0.419
SDSS $g − i$	−0.341	0.180	−0.077	0.768
Optical disc inclination	0.259	0.315	0.102	0.697
AGES spectrum mean S/N	−0.312	0.222	−0.246	0.340
AGES H I offset $> 2\sigma$				
Subcluster distance	0.256	0.447	0.391	0.235
H I deficiency	0.099	0.772	0.000	1.000
H I mass	0.038	0.910	0.200	0.555
SDSS $g − i$	0.333	0.316	0.300	0.370
Optical disc inclination	0.012	0.972	0.291	0.385
AGES spectrum mean S/N	−0.046	0.894	−0.041	0.905

Note. [a]Relations in bold typeface are those for which a onetailed directional test using the Pearson r rejects the null hypothesis that the variables are uncorrelated at confidence levels of 95 per cent or greater. The degrees of freedom for the tests is 15, i.e. sample size −2. The H I deficiencies and H I mass were calculated assuming a distance to the cluster of 92 Mpc.
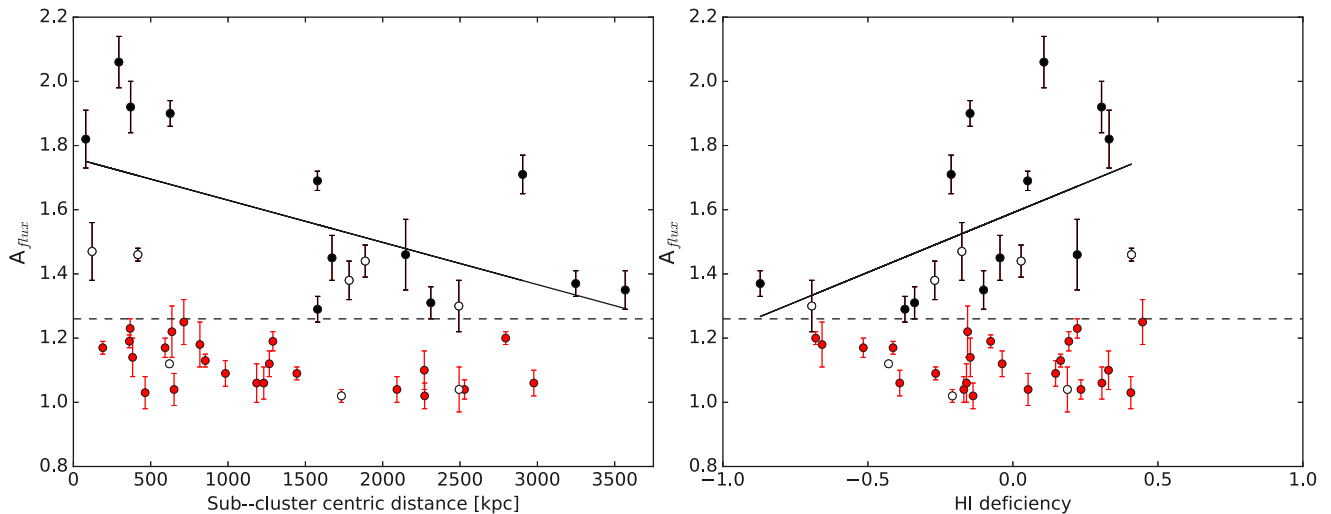
Figure 4. A_{flux} ratio versus subcluster distance and H I deficiency for LTGs in the A1367 volume. LTGs with $A_{flux} > 2\sigma$ are shown with black symbols and those with $A_{flux} < 2\sigma$ with red symbols. Left: A_{flux} ratio versus subcluster distance. The solid line shows the least-squares fit for LTGs with $A_{flux} > 2\sigma$, i.e. a fit exclusively to the black symbols, i.e. those above the dashed line. Right: A_{flux} ratio versus H I deficiency. The solid line is a least-squares fit for LTGs with an $A_{flux} > 2\sigma$, i.e. a fit exclusively to the black symbols, i.e. above the dashed line. The open symbols indicate LTGs which are members of close pairs or groups and the dashed horizontal line indicates the A_{flux} 2σ level from the AMIGA isolated galaxy sample.

maps of nearby LTGs available from the THINGS[16] online archive. Our analysis of the THINGS H I offsets was carried out after convolving the THINGS ROBUST = 0 H I maps with a 90 arcsec beam, using the AIPS task CONVL, to compensate for the greater distance at which the A1367 galaxies were observed. Fig. 6 shows histograms of the projected H I offset magnitudes (normalized by R_{25}) for the A1367 and THINGS LTGs. Table 7 shows the median and mean of these normalized H I offset values. The median normalized resolved VLA H I offsets for the A1367 and THINGS galaxies are 0.27 and 0.23 with mean values of 0.27 ± 0.15 and 0.33 ± 0.38, respectively.

Inspection of the high-resolution THINGS H I images reveals that they have widely diverse morphologies, with the H I intensity maxima variously associated with H I central concentrations, rings, spiral arms, and tidal features in ways that do not follow an easily predictable pattern. This is reflected in the large standard deviation from the mean offset for the R_{25} normalized resolved H I offsets for the THINGS galaxies. Within the limitations of the small sample sizes and large variation in H I offset magnitudes, the mean R_{25} normalized resolved VLA H I offset in the A1367 galaxies cannot be distinguished from those in the THINGS galaxies (i.e. LTGs near the Virgo cluster outskirts).

5.3.3 Unresolved (AGES) versus resolved VLA H I offsets

For 21 galaxies in the A1367 volume, we have both an AGES H I position and a resolved VLA H I column density maximum position from the VLA maps. However, neither the magnitudes of the

[16] The H I Nearby Galaxy Survey (Walter et al. 2008). M 81 was excluded from our THINGS sample because of incomplete continuum subtraction from its H I map in the archive.
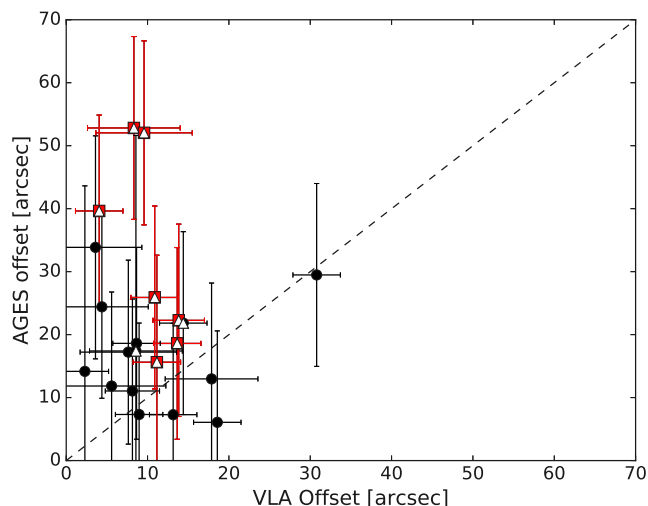
Figure 5. Magnitude of the resolved VLA versus AGES unresolved H I offsets in arcseconds. Galaxies displaying resolved H I morphologies with distinct one sided H I tails are plotted with red square symbols and those with $A_{flux} > 2\sigma$ are shown with a white triangle. The dashed lined indicates where the 1:1 relationship lies.

Table 6. AGES H I offsets in the A1367 volume.

H I offsets from AGES H I positions	Total[a]	offset $>3\sigma$	offset $>2\sigma$	offset $>1\sigma$
Number of galaxies	43	4	11	26
Percentage		9	26	60

Note. [a]Excludes four AGES galaxies with spectra significantly impacted by RFI.
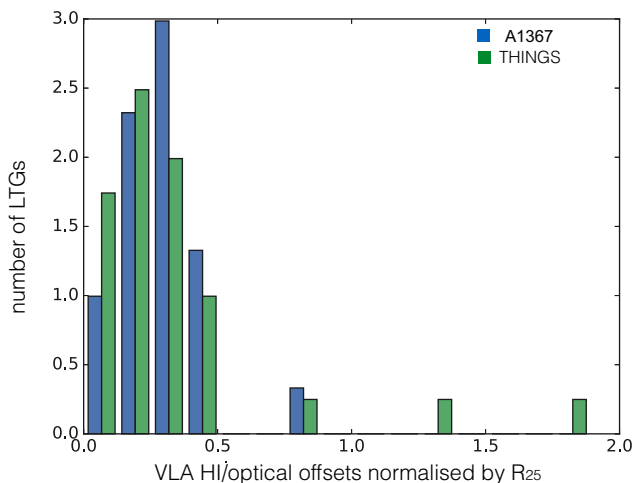
Figure 6. Comparative distribution of the number of LTGs (vertical axis) versus their H I projected offset magnitudes, normalized by their R_{25}, derived from resolved VLA A 1367 and THINGS H I maps (horizontal axis).

offsets nor the offset orientations from AGES and the VLA were statistically correlated. In both cases, the null hypothesis that the variables are uncorrelated was accepted (one-tailed test) at confidence levels of 99.95 per cent, with the Pearson r and the p-values for offset magnitude being $r(\mathrm{df} = 19) = -0.123, p = 0.5964$, and for orientation, $r(\mathrm{df} = 19) = 0.268, p = 0.240$. Fig. 5 shows the projected magnitude of the AGES and resolved VLA H I offsets in arcseconds for the 21 galaxies. The mean AGES H I off-

Table 7. Magnitude H I offsets normalized by optical R_{25}.

H I maxima	Survey	Median	Mean	n^a
Resolved (VLA)	A 1367[b]	0.27	0.27 ± 0.15	29
Resolved (VLA)	THINGS[c]	0.23	0.33 ± 0.38	32
Unresolved (Arecibo)	AGES	0.52	0.79 ± 0.74	43

Notes. [a]Number of H I detections with optical counterparts.
[b]R_{25} is from, in order of preference, Hyperleda, NED, and our own estimate from SDSS images.
[c]R_{25} is from $D_{25}/2$ from Walter et al. (2008).

set (22 ± 13 arcsec) is twice the mean resolved VLA H I offset (11 ± 6 arcsec).

As part of trying to understand the reason for this difference, we investigated the impact of spatial resolution on the position of the H I maxima. We used the AIPS task CONVL to progressively smooth the highest resolution H I images available, i.e. THINGS H I maps of nearby galaxies. Progressively increased smoothing of the THINGS maps in almost all cases significantly changed the position of the H I maximum intensity away from the highest column density clumps resolvable in the THINGS images towards the flux-weighted mean position of the H I in the whole galaxy. Fig. 7 illustrates the effect of resolution on the position of H I maximum intensity. For the THINGS galaxies, the mean shift in H I maximum intensity between the images smoothed with 15 and 210 arcsec beams was 94 arcsec. From this, we conclude the unresolved AGES A1367 H I positions reflect the flux-weighted mean position of each map's H I, whereas its resolved VLA H I column density maximum locates the highest density H I within the resolved map's resolution limit. Moreover, our analysis in Section 5.3.2 indicates that for highly resolved maps the position of the H I column density maximum offset has a large natural variation. The THINGS results explain why for the A1367 LTGs, the VLA H I offsets are not correlated with the AGES H I offsets or other lower density resolved H I morphology or kinematic perturbation signatures, even in cases where the resolved maps show only some moderate H I perturbation.

On the other hand, the THINGS results suggest that the unresolved AGES H I offsets can reflect the effect of interactions which have asymmetrically displaced significant masses of lower density H I with little or no impact on any offset derived on the basis of the resolved VLA H I maps. This naturally explains why all of the LTGs with clearly identifiable diffuse one-sided H I tails (e.g. FGC 1287 and CGCG 097−087; Fig. A7), shown with red squares in Fig. 5, have larger AGES H I offsets than VLA H I offsets. A good example is CGCG 097−062, a galaxy with both optical and H I one-sided SE-oriented tails. Table 4 reveals it has an AGES H I offset $> 2\sigma = 39.6 \pm 15.2$ (16 kpc), but its H I column density maximum in the VLA C-array map is projected at the optical centre, as seen in Fig. A2 in Appendix A. Other examples showing a low-density one-sided H I tail, but no significant resolved VLA H I offset, are CGCG 097−121 and CGCG 097−102 (see Appendix A, including Figs A11 and A10).

5.4 A_{flux} distribution: comparison with the Virgo cluster

In an effort to understand whether the H I in A1367 LTGs is more perturbed than in other nearby clusters, we defined a cluster volume for Virgo (RA [11:55:22, 13:06:10], Dec. [3:28:12, 21:12:00], and V[−1000, 3000]). This cluster volume was calculated by scaling the Virgo cluster volume relative to the dimensions of the A1367–AGES volume, i.e. $1.64 \times R_{200}$ and a velocity range $\sim 4\times$ the cluster's velocity dispersion. A substantial fraction of the Virgo
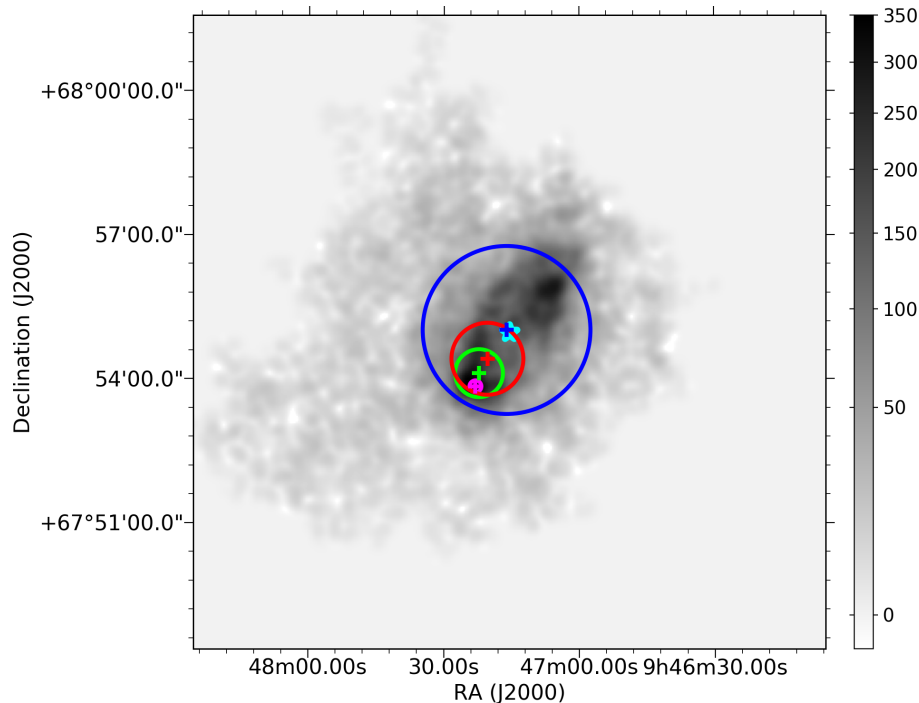
Figure 7. NGC 2976 ($V_{hel} = 3 \, \mathrm{km \, s^{-1}}$) THINGS H I map showing the impact of resolution on the position of the H I intensity maximum. The crosses mark the positions of the H I intensity maxima from maps smoothed with the AIPS tasks CONVL using beam sizes of 15 (magenta), 60 (green), 90 (red), and 210 (blue) arcsec. The circles of the same colour indicate the CONVL beam size, with the 210 arcsec beam approximately equal to the Arecibo 3.5 arcmin FWHP beam. The cyan star marks the optical centre of the galaxy. The grey scale shows the H I column density in the figure in units of 10^{19} atoms cm^2.

volume defined in this way is included within the ALFALFA blind H I surveys (Giovanelli et al. 2007; Kent et al. 2008) and like the AGES survey for A1367, these surveys were carried out with the ALFA receiver and the Arecibo 305-m telescope. From here on we refer to the ALFALFA surveyed portion of the Virgo volume as the Virgo–ALFALFA volume.

We compiled a sample of 220 spectra for H I detections within the Virgo–ALFALFA volume which have optical counterparts and spectra of high quality (quality parameter = 1) in Giovanelli et al. (2007) and Kent et al. (2008). After reviewing the notes for these ALFALFA surveys, we excluded 11 of these spectra because they were noted as being contaminated by RFI or confused with another sources. We retrieved the remaining sample spectra, with the exception of two spectra that were unavailable, from the NED ALFALFA data archive (Haynes et al. 2011), i.e. a final sample of 207 spectra. Although using observations from the same telescope aids comparability of the spectra, because Virgo is closer than A1367 the Virgo–ALFALFA sample has a lower H I mass detection threshold. To ensure a proper comparison between the distribution of A_{flux} in Virgo and A1367, we selected only Virgo–ALFALFA spectra for galaxies with $M(\mathrm{H \, I}) > 3 \times 10^8 \, \mathrm{M_\odot}$, i.e. the lowest H I mass LTG in our A1367–AGES sample; 90 of the 207 Virgo–ALFALFA sample galaxies met this criteria.

We determined A_{flux} for the 90 Virgo–ALFALFA spectra and the distribution of their A_{flux} ratios is shown in Fig. 2 (lower panel) compared to the half Gaussian fit to the A_{flux} distribution from the AMIGA sample of isolated galaxies (Espada et al. 2011). 14 (16 per cent) of the Virgo–ALFALFA galaxies ($M(\mathrm{H \, I}) > 3 \times 13^8$ $\mathrm{M_\odot}$) have $A_{flux} > 3\sigma$ (1.39) in the AMIGA sample. This compares to 26 per cent for A1367. The mean A_{flux} uncertainty for the Virgo–ALFALFA and A1367–AGES samples are 0.07 and 0.05, respectively. We also examined the distribution of A_{flux} ratios for

the 117 Virgo–ALFALFA galaxies excluded from the sample of 90 galaxies solely because their $M(\mathrm{H \, I})$ was $\leq 3 \times 10^8 \, \mathrm{M_\odot}$. 49 (42 per cent) of these galaxies have $A_{flux} > 3\sigma$ (1.39) in the AMIGA sample.

The VIVA[17] VLA H I imaging survey of Virgo galaxies revealed five galaxies and an interacting pair with long one-sided H I tails (Chung et al. 2007). All of these galaxies except NGC 4424 have an H I mass $>3 \times 10^8 \, \mathrm{M_\odot}$. Three of the five galaxies (NGC 4654, NGC 4302, and NGC 4330) had A_{flux} from their ALFALFA spectra $> 2\sigma$ from the AMIGA sample distribution (1.26). For the pair (NGC 4294/4299), which have a projected separation of 5.6 arcmin, only the higher inclination member, NGC 4294, has an ALFALFA $A_{flux} > 1.26$. We conclude that $A_{flux} > 1.26$ is associated with a majority of VIVA galaxies with long H I tails, but it is not the case for all of them.

For the Virgo and A1367 samples uncertainties about the fraction of galaxies with $A_{flux} > 1.39$ are introduced by the process of selecting eligible spectra, e.g. because of Arecibo's fixed FWHP beam size and the greater distance to A1367, H I detections are more likely to be confused than those in the nearer isolated and Virgo samples. For the parts of the A1367 volume where we have VLA H I data we were able to correct for this by substituting unconfused VLA A_{flux} values (CGCG 097−068 and CGCG 097−125), but in the rest of the A1367 volume we cannot rule out confusion.

Even allowing for possible confusion, the comparison between distribution of A_{flux} values from the A1367 and Virgo samples with $M(\mathrm{H \, I}) > 3 \times 10^8 \, \mathrm{M_\odot}$ provides clear evidence of a higher frequency of strong H I profile perturbations in A1367 LTGs. Also, the higher fraction of Virgo galaxies with A_{flux} above the AMIGA 3σ value in the lower H I mass sample compared to the fraction from the

---

[17] VLA Imaging of Virgo galaxies in Atomic gas.

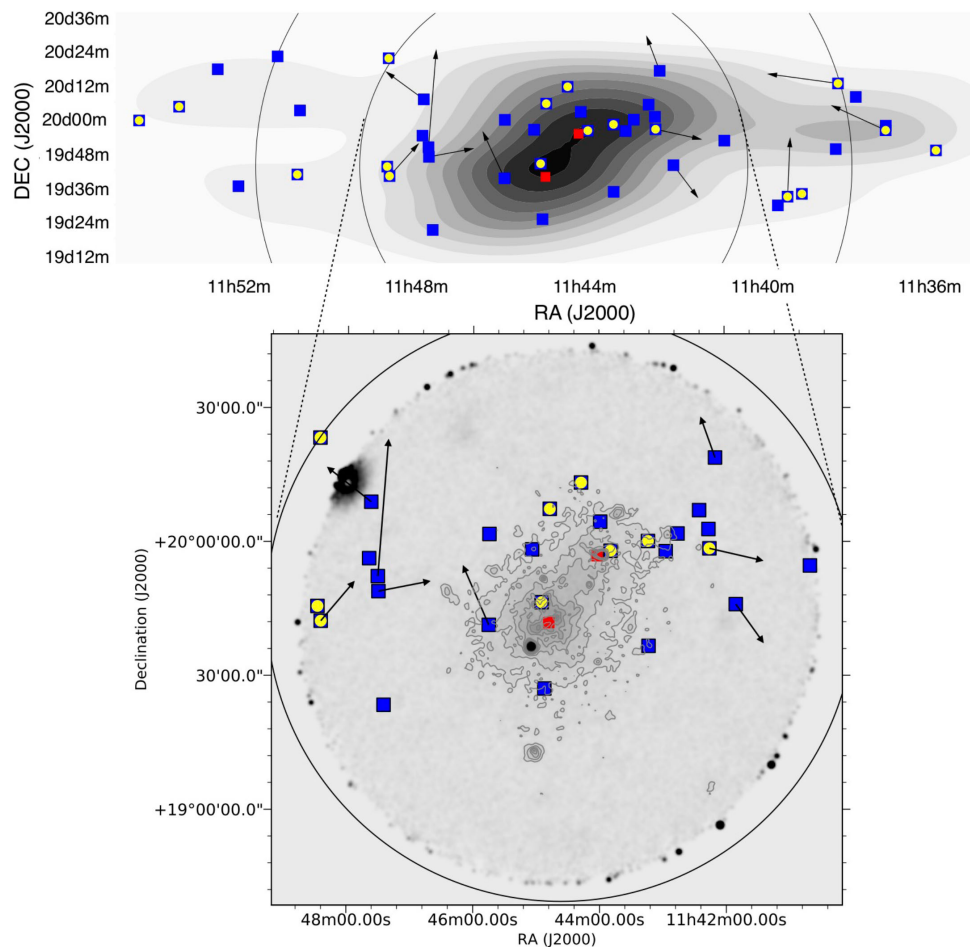**Figure 8.** Top panel: A1367 positions of galaxies with $A_{flux} > 2\sigma$ (yellow dots), projected offset magnitudes ($\times 20$) and orientations of the AGES H I offsets $> 2\sigma$ (black arrows) and the 43 AGES H I detections (blue squares). Positions projected on grey-scale contours from a density map for all galaxies with SDSS spectroscopic redshifts in the A1367 volume. Lower panel: zoom-in of the data projected on a *ROSAT* X-ray image with grey contours. The red squares indicate the location of the SE and NW subcluster cores (Donnelly et al. 1998). The outer larger circle is the virial radius and the inner larger circle is the R_{200} radius.

higher H I mass sample, suggests the lower H I mass galaxies are preferentially perturbed. However, this higher fraction of lower H I mass galaxies in Virgo is also, to some extent, probably due to the presence of perturbed residual H I in high stellar mass galaxies at a late stage of gas stripping.

5.5 ICM and galaxy density

Modelling (e.g. Tonnesen 2007) supports the general proposition that ram-pressure stripping is the principal mechanism for gas loss in nearby cluster LTGs. But in A1367, ram-pressure stripping modelling reported in Paper I for velocities approximately equal to the cluster velocity dispersion, suggests most of its LTGs are only subject to moderate ram pressure, except within ∼200 kpc of the subcluster cores. Clumpy ICM, shocks, and bulk ICM motions could potentially enhance ram pressure by up to an order of magnitude (Kenney, van Gorkom & Vollmer 2004). However, we see no evidence of ICM clumps at the sensitivity and resolution of available *ROSAT* and *XMM–Newton* X-ray data. Projection effects may mask a preferred direction for AGES H I offsets. However, if the AGES H I offsets are due to a systematic, as opposed to a sudden increase in ram-pressure stripping during their infall, we would expect the

projected magnitude of the H I offsets to increase with proximity to the cluster centre. However, we do not see evidence of this in Fig. 8.

Fig. 8 shows the AGES H I offsets $> 2\sigma$ (black arrows) and $A_{flux} > 2\sigma$ (yellow filled circles) projected against galaxy density and ICM X-ray emission (*ROSAT*) as well as the 43 AGES H I detections (blue squares). The LTGs with $A_{flux} > 2\sigma$ are projected more or less randomly within the regions in the A1367 volume enclosed by the lowest galaxy density contour. On the other hand, the AGES H I offsets $> 2\sigma$ appear preferentially projected at cluster-centric radii about half of the R_{200} radius. We do not see any clear correlation between either of the AGES H I offsets or $A_{flux} > 2\sigma$ and either galaxy density or ICM density traced by X-ray emission. It is important to not confuse the lack of correlation with projected position for LTGs having $A_{flux} > 2\sigma$ in Fig. 8 with the correlation between cluster centric distance and the magnitude of $A_{flux} > 2\sigma$ shown in Fig. 3.

6 CONCLUDING REMARKS

Using the single-dish and resolved H I data available to us for A1367 LTGs, including VLA C-configuration data for the 16 objects presented in this paper, we analysed four types of H I perturbation signature (H I profile asymmetries, H I velocity offsets as well as

projected resolved and unresolved H I position versus optical position offsets).

(i) 26 per cent of A 1367 LTGs have asymmetric AGES H I profiles with an A_{flux} ratio greater than the 3 times the 1σ dispersion in the ratio (3σ for short) from a sample of isolated galaxies. Only $\sim$2 per cent of the isolated sample have an A_{flux} ratio greater than its 3σ value and for other samples probing denser environments the fractions are between 10 per cent and 20 per cent.

(ii) For the A1367 LTGs, there is a statistically significant correlation between their $A_{flux} > 2\sigma$ from AGES and both their proximity to the subcluster centres and their H I deficiency. This indicates $A_{flux} > 2\sigma$ from AGES can be a signature of recent or ongoing H I stripping; 56 per cent of the A1367 LTGs, which are members of groups or pairs, have an A_{flux} ratio $> 2\sigma$. These groups and pairs of LTGs make up 31 per cent of the A1367 LTGs with an A_{flux} ratio $> 2\sigma$. This suggests interactions between group or pair members may significantly contribute to the number of A1367 galaxies displaying an A_{flux} ratio $> 2\sigma$.

(iii) For A1367 LTGs, we did not find a statistically significant correlation between A_{flux} magnitudes $> 2\sigma$ and the magnitudes of AGES H I offsets $>$ the 2σ pointing error. However, in cases where both of these signatures are present and the resolved VLA H I mapping is available, the resolved H I morphology, and kinematics confirm a strongly perturbed H I disc.

(iv) For the 19 A 1367 LTGs for which we have both AGES offsets and resolved VLA H I offsets. No statistical correlation was found for either the H I offset magnitudes or orientations from the two telescopes. However, the mean resolved VLA H I offset magnitude is only about half that of the mean resolved AGES H I offset. The LTGs with the most extreme differences between their AGES and VLA H I offset magnitudes are those where the VLA H I maps reveal low-density one-sided H I tails, but with little or no evidence of an impact on the highest density H I from the resolved H I offsets. This suggests that the AGES H I offsets $> 2\sigma$ pointing uncertainties are sensitive to interactions which asymmetrically displace significant masses of low-density H I.

(v) The 26 per cent of A1367 LTGs with $A_{flux} > 3\sigma$ in an isolated sample, compares to 16 per cent from a comparable sample of Virgo galaxies drawn from the ALFALFA blind H I surveys. These fractions indicate a higher frequency of strong H I perturbations in A1367 LTGs in comparison to Virgo.

(vi) Within the A1367 volume, the projected distribution of neither the LTGs with unresolved AGES H I offsets, $> 2\sigma$ pointing uncertainties, nor those with an A_{flux} ratio $> 2\sigma$ display a clear correlation with distance from the cluster centre, galaxy density or the cluster's ICM X-ray emission (*ROSAT*).

This study confirms that the A1367 LTGs are suffering ongoing strong and widespread interactions which are significantly perturbing their H I. While the evidence so far reveals examples which are consistent with ram-pressure stripping and/or tidal interactions, determining (with greater certainty) the dominant interaction mechanism for each galaxy and for the cluster as whole will require further detailed multiwavelength studies and modelling.

ACKNOWLEDGEMENTS

REFERENCES

Amram P., Gavazzi G., Marcelin M., Boselli A., Vílchez J. M., Iglesias-Paramo J., Tarenghi M., 2002, Ap&SS, 281, 401
Bekki K., 2014, MNRAS, 438, 444
Boselli A., Gavazzi G., 2006, PASP, 118, 517
Boselli A., Gavazzi G., Combes F., Lequeux J., 1994, A&A, 285, 69
Boselli A., Boissier S., Cortese L., Gil de Paz A., Seibert M., Madore B. F., Buat V., Martin D. C., 2006, ApJ, 651, 811
Boselli A., Cortese L., Boquien M., Boissier S., Catinella B., Gavazzi G., Lagos C., Saintonge A., 2014, A&A, 564, A67
Boselli A. et al., 2016, A&A, 587, A68
Bravo-Alfaro H., Cayatte V., van Gorkom J. H., Balkowski C., 2000, AJ, 119, 580
Briggs D. S., 1995, BAAS, 27, 1444
Brown T. et al., 2017, MNRAS, 466, 1275
Chung A., van Gorkom J. H., Kenney J. D. P., Vollmer B., 2007, ApJ, 659, L115
Chung A., van Gorkom J. H., Kenney J. D. P., Crowl H., Vollmer B., 2009, AJ, 138, 1741
Conselice C. J., 2003, ApJS, 147, 1
Consolandi G., Gavazzi G., Fossati M., Fumagalli M., Boselli A., Yagi M., Yoshida M., 2017, A&A, 606, A83
Cortese L., Gavazzi G., Boselli A., Iglesias-Paramo J., Carrasco L., 2004, A&A, 425, 429
Cortese L., Gavazzi G., Boselli A., Franzetti P., Kennicutt R. C., O'Neil K., Sakai S., 2006, A&A, 453, 847
Cortese L. et al., 2008, MNRAS, 383, 1519
Cortese L. et al., 2012, A&A, 544, A101
Di Teodoro E. M., Fraternali F., 2015, MNRAS, 451, 3021
Dickey J. M., Gavazzi G., 1991, ApJ, 373, 347
Domínguez M., Muriel H., Lambas D. G., 2001, AJ, 121, 1266
Donnelly R. H., Markevitch M., Forman W., Jones C., David L. P., Churazov E., Gilfanov M., 1998, ApJ, 500, 138
Dressler A., 2004, in Mulchaey J. S., Dressler A., Oemler A., eds, Clusters of Galaxies: Probes of Cosmological Structure and Galaxy Evolution. Cambridge Univ. Press, Cambridge, p. 206
Espada D., Verdes-Montenegro L., Huchtmeier W. K., Sulentic J., Verley S., Leon S., Sabater J., 2011, A&A, 532, A117
Fasano G., Poggianti B. M., Couch W. J., Bettoni D., Kjærgaard P., Moles M., 2000, ApJ, 542, 673
Fossati M., Fumagalli M., Boselli A., Gavazzi G., Sun M., Wilman D. J., 2016, MNRAS, 455, 2028
Gavazzi G., 1989, ApJ, 346, 59
Gavazzi G., Jaffe W., 1987, A&A, 186, L1
Gavazzi G., Contursi A., Carrasco L., Boselli A., Kennicutt R., Scodeggio M., Jaffe W., 1995, A&A, 304, 325

Gavazzi G., Marcelin M., Boselli A., Amram P., Vílchez J. M., Iglesias-Paramo J., Tarenghi M., 2001a, A&A, 377, 745

Gavazzi G., Boselli A., Mayer L., Iglesias-Paramo J., Vílchez J. M., Carrasco L., 2001b, ApJ, 563, L23

Gavazzi G., Boselli A., Donati A., Franzetti P., Scodeggio M., 2003, A&A, 400, 451

Giovanelli R. et al., 2005, AJ, 130, 2598

Giovanelli R., Haynes M. P., Kent B. R., Saintonge A., Stierwalt S., Altaf A., 2007, AJ, 133, 2569

Goto T., Yamauchi C., Fujita Y., Okamura S., Sekiguchi M., Smail I., Bernardi M., Gomez P. L., 2003, MNRAS, 346, 601

Gunn J. E., Gott J. R. I., 1972, ApJ, 176, 1

Haynes M. P., Giovanelli R., 1984, AJ, 89, 758

Haynes M. P., Giovanelli R., Kent B. R., 2007, ApJ, 665, L19

Haynes M. P. et al., 2011, AJ, 142, 170

Hess K. M., Wilcots E. M., 2013, AJ, 146, 124

Jaffé Y. L., Smith R., Candlish G. N., Poggianti B. M., Sheen Y.-K., Verheijen M. A. W., 2015, MNRAS, 448, 1715

Kenney J. D. P., van Gorkom J. H., Vollmer B., 2004, AJ, 127, 3361

Kent B. R. et al., 2008, AJ, 136, 713

Koopmann R. A., Kenney J. D. P., 2004, ApJ, 613, 851

Makarov D., Prugniel P., Terekhova N., Courtois H., Vauglin I., 2014, A&A, 570, A13

Montes M., Trujillo I., 2014, ApJ, 794, 137

Moore B., Katz N., Lake G., Dressler A., Oemler A., 1996, Nature, 379, 613

Moss C., 2006, MNRAS, 373, 167

Plionis M., Tovmassian H. M., Andernach H., 2009, MNRAS, 395, 2

Poggianti B. M., Aragón-Salamanca A., Zaritsky D., De Lucia G., Milvang-Jensen B., Desai V., Jablonka P., 2009, ApJ, 693, 112

Robitaille T., Bressert E., 2012, Astrophysics Source Code Library, record ascl:1208.017

Roediger E., Hensler G., 2005, A&A, 433, 875

Sakai S., Kennicutt R. C. Jr, van der Hulst J. M., Moss C., 2002, ApJ, 578, 842

Scott T. C. et al., 2010, MNRAS, 403, 1175 (Paper I)

Scott T. C., Cortese L., Brinks E., Bravo-Alfaro H., Auld R., Minchin R., 2012, MNRAS, 419, L19 (Paper II)

Scott T. C., Usero A., Brinks E., Boselli A., Cortese L., Bravo-Alfaro H., 2013, MNRAS, 429, 221 (Paper III)

Scott T. C., Usero A., Brinks E., Bravo-Alfaro H., Cortese L., Boselli A., Argudo-Fernández M., 2015, MNRAS, 453, 328 (Paper IV)

Sengupta C., Dwarakanath K. S., Saikia D. J., Scott T. C., 2013, MNRAS, 431, L1

Sengupta C., Scott T. C., Paudel S., Saikia D. J., Dwarakanath K. S., Sohn B. W., 2015, A&A, 584, A114

Skrutskie M. F. et al., 2006, AJ, 131, 1163

Solanes J. M., Manrique A., García-Gómez C., González-Casado G., Giovanelli R., Haynes M. P., 2001, ApJ, 548, 97

Spergel D. N. et al., 2007, ApJS, 170, 377

Tonnesen S., 2007, New Astron. Rev., 51, 80

van Gorkom J. H., 2004, in Mulchaey J. S., Dressler A., Oemler A., eds, Clusters of Galaxies: Probes of Cosmological Structure and Galaxy Evolution. Cambridge Univ. Press, Cambridge, p. 305

Venkatapathy Y. et al., 2017, AJ, 154, 227

Vollmer B., Braine J., Pappalardo C., Hily-Blant P., 2008, A&A, 491, 455

Walter F., Brinks E., de Blok W. J. G., Bigiel F., Kennicutt Jr R. C., Thornley M. D., Leroy A., 2008, AJ, 136, 2563

Yagi M., Yoshida M., Gavazzi G., Komiyama Y., Kashikawa N., Okamura S., 2017, ApJ, 839, 65

Yoon H., Chung A., Smith R., Jaffé Y. L., 2017, ApJ, 838, 81

Zwicky F., Herzog E., Wild P., 1968, Catalogue of Galaxies and of Clusters of Galaxies. California Institute of Technology, Pasadena

APPENDIX A: VLA C-ARRAY H I DETECTIONS

This appendix presents the velocity integrated H I maps and H I velocity fields for the galaxies and extragalactic H II region listed in Table 2. A brief analysis is also presented for each galaxy. In each case we comment, from the available data, on the evidence for or against a perturbed old stellar disc as an indication of a recent tidal interaction. Limitations on the use of NIR images for assessing perturbations of old stellar populations are considered in Paper IV. The galaxies are presented in ascending RA order.

CGCG 127−032: Fig. A1 shows H I detected in two elongated clumps S and NE of the optical centre. This irregular H I morphology contrasts strongly with the symmetric face-on optical spiral with two prominent spiral arms which encircle the galaxy in a rather symmetric way. CGCG 127−032 has an AGES H I offset of 29.5 ± 14 arcsec which is consistent with the resolved VLA H I morphology. The maximum H I column density in the map was 3.8×10^{20} atoms cm^{-2}. Unfortunately, the best available NIR images for the galaxy are not deep enough to determine whether the old stellar disc edge is perturbed or not.

CGCG 097−062: this galaxy displays a cometary optical morphology with its tail oriented to the SE. As the left-hand panel of Fig. A2 shows, the highest column density H I (1.7×10^{21} atoms cm^{-2}) is projected at the optical centre with a lower column density H I counterpart to the optical tail, extending to the star projected at the end of the optical tail. See also Section 5.3.3. The H I velocity field contours in the right-hand panel of the figure show regular rotation across the brightest part of the optical disc, but signs of a warp along the tail. CGCG 097−062 shows clear signs of perturbation of the H I in the outer disc most probably caused by the same mechanism that produced the optical tail. There are counterparts to the tail in the *J*-, *H*,- and *K*-band 2MASS images. The H I maps for this galaxy are based on NRAO VLA archival data rather than our own observations (see Appendix B2).

CGCG 097−063: its column density maximum (1.3×10^{21} atoms cm^{-2}) is aligned, within the pointing uncertainties, with the optical centre (Fig. A3, left-hand panel). The SE disc edge in a smoothed SDSS *z*-band image is elongated compared to the NW and curves sharply south towards the disc edge. The velocity field (Fig. A3, right-hand panel) isovelocity contours are perpendicular to the optical disc major axis with a slight hint of perturbation at the SE optical disc edge.

CGCG 097−068: this gas-rich (H I deficiency −0.3, Table 2) Sc galaxy shows several H I morphological and kinematic ongoing interaction signatures: (i) in projection the H I 3σ contour in Fig. A4 (left-hand panel) extends ∼58 arcsec (24 kpc) north of the optical centre (perpendicular to the major axis), more than twice ∼26 arcsec (11 kpc) it extends in the opposite direction. This confirms the earlier reports of an asymmetric H I morphology in Dickey & Gavazzi (1991) and Paper I; (ii) H I column densities rise much more rapidly south of the optical centre than to the north of it; (iii) an eastern H I extension reaches the projected position of a smaller Irr cluster galaxy, SDSS J114229.18+200713.7; (iv) in the H I velocity field (Fig. A4, right-hand panel) there is a systematic change in the of the angle H I isovelocity lines, relative to the major optical axis indicating stronger warping of the H I disc at its eastern edge compared to the western edge; (v) FUV and NUV *(GALEX)* images show CGCG 097−068 to have an extended UV disc (XUV disc) with a similar extent to the H I disc, except in the eastern H I extension. The column density maximum (2.6×10^{21} atoms cm^{-2}) is offset 18.6 ± 2.9 arcsec (7.7 kpc) W of the optical centre. Smoothed *Spitzer* 3.6- and 4.5-µm images suggest an extension of diffuse NIR emission at the NE disc edge, possibly due to an interaction with SDSS J114229.18+200713.7. This small companion only
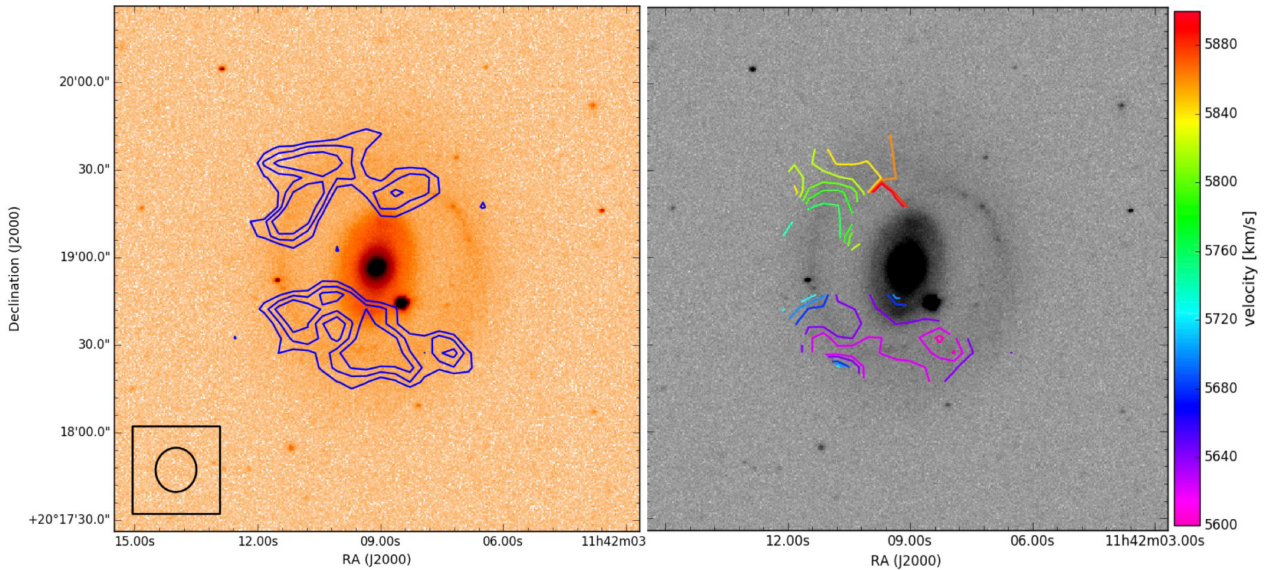
Figure A1. CGCG 127−032, left: H I integrated intensity contours from the PBCOR corrected map with contours at 1.6, 2.1, and 2.6 × 10²⁰ atoms cm⁻². Right: H I velocity field with velocities of the contours corresponding to the colour scale at the right of the figure. The separation between contours, unless noted otherwise, is 20 km s⁻¹. The boxed ellipse indicates the size of the VLA synthesized C-array beam. The background for both maps is an SDSS *g*-band image.
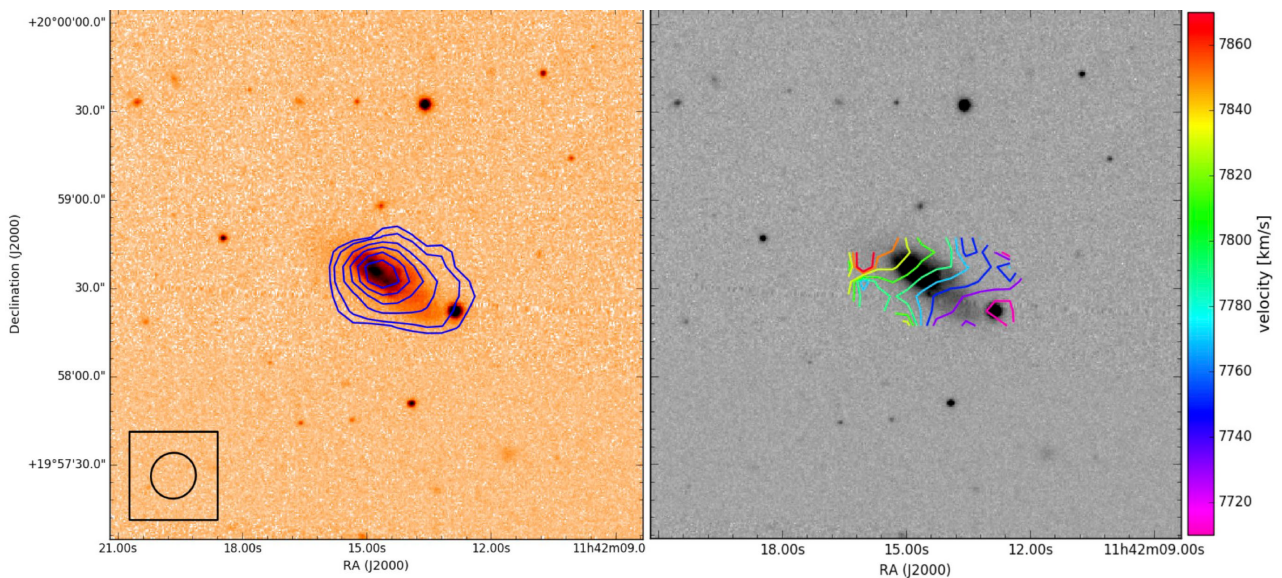

Figure A2. CGCG 097−062, left: H I integrated intensity contours at 1.7, 2.9, 5.8, 8.7, 11.6 and 14.6 × 10²⁰ atoms cm⁻². Other details are per Fig. A1.

has ∼1 per cent of CGCG 097−068's stellar mass and an optical systemic velocity ∼259 km s⁻¹ greater than CGCG 097−068. An alternative interpretation is that the large-scale H I asymmetries in CGCG 097−068, including the warp, are caused by ram pressure as the galaxy's ISM interacts with the ICM on a south westerly trajectory. In this scenario, the eastern H I extension would be explained as being similar to that seen in the classic ram-pressure stripping case NGC 4522.

CGCG 097−072: the integrated H I map for CGCG 097−072 (Fig. A5) shows the H I disc is truncated to approximately the radius of the optical disc consistent with its H I deficiency of 0.5 (Table 2), although it has an H₂ excess of −0.20 (Paper III). Its H I column density maximum in the VLA C-array map (8.2 × 10²⁰ atoms cm⁻²) is offset 8.6 ± 2.9 arcsec (3.6 kpc) SE of the optical centre.

An overall rotation pattern is seen in the velocity field in the right-hand panel of the figure, but there is also evidence of perturbed H I kinematics and morphology north of the H I column density maximum. Smoothed *Spitzer* 3.6- and 4.5-µm band images show perturbation signatures near the western edge of the disc, which are possibly the result of a tidal perturbation of the outer disc within the relaxation time-scale, which is assumed to be approximately the time for a single disc rotation,[18] i.e. ∼0.4 Gyr, based on W_{20} from Table 2.

SDSS J114250.97+202631.8: Fig. A6 shows the integrated H I map for this galaxy, which is projected ∼840 kpc from the NW

---

[18] T_{rot} (Gyr) = 6.1478 r/ V_{rot}, where r = the optical radius (kpc) and V_{rot} = 0.5 ΔV (km s⁻¹)/sin(*i*).
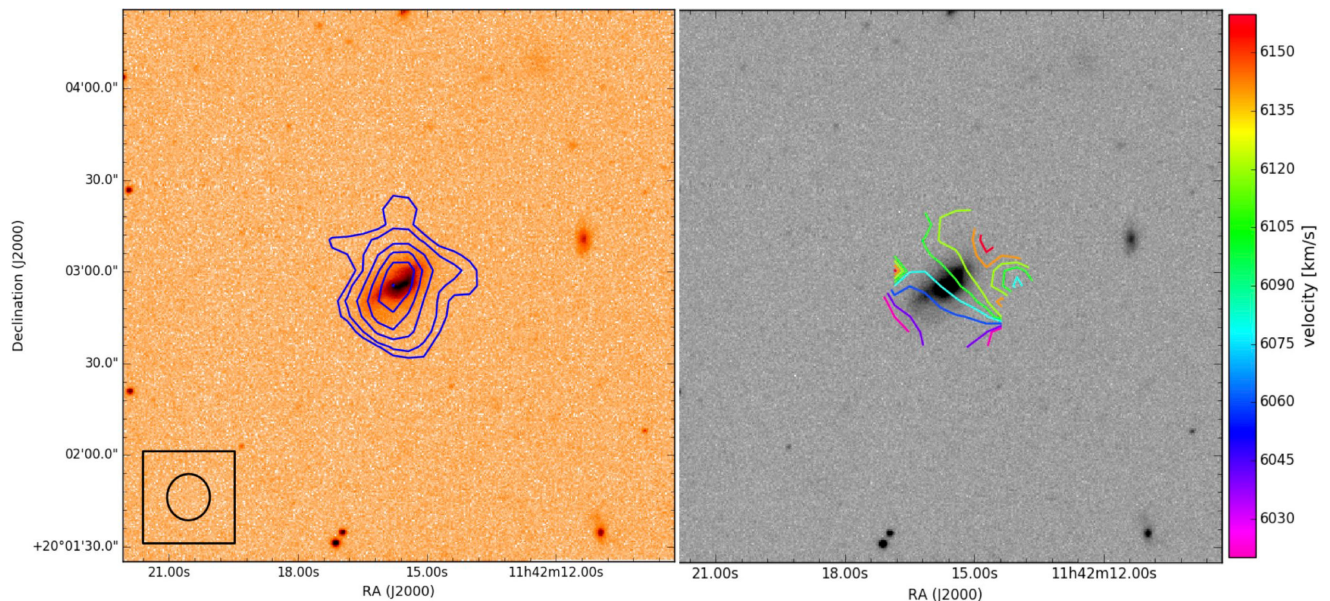
Figure A3. CGCG 097−063, left: H I integrated intensity contours at 1.6, 2.6, 5.2, 7.8, and 10.4 × 10²⁰ atoms cm⁻². Other details are per Fig. A1.
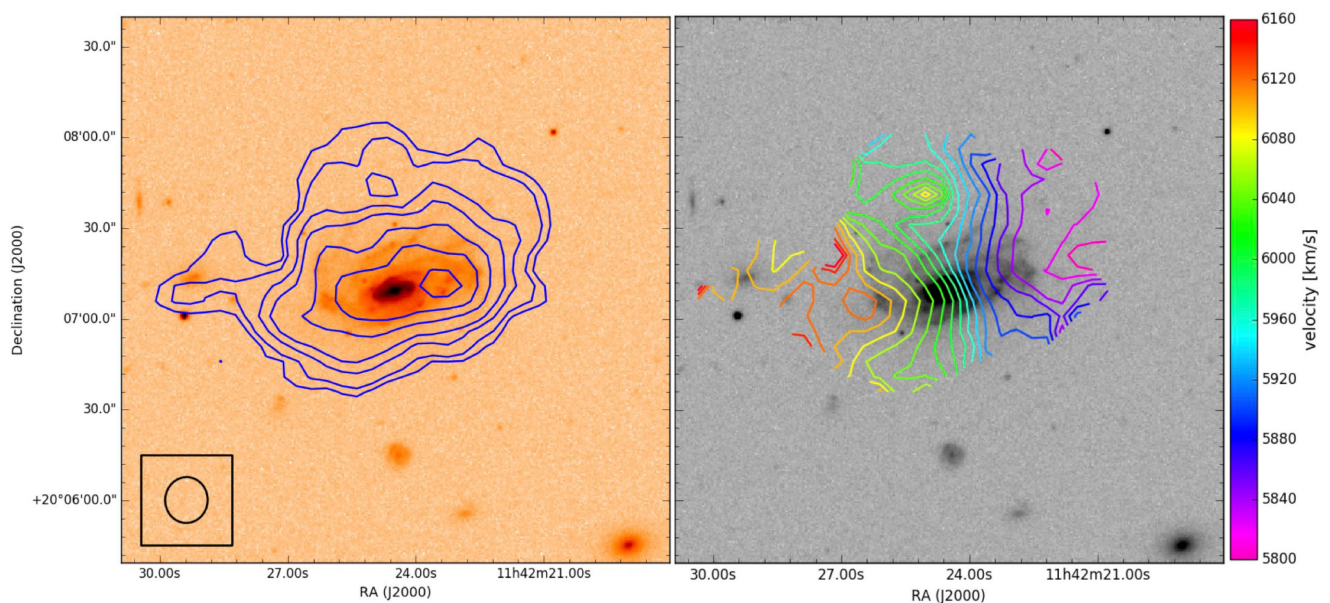

Figure A4. CGCG 097−068, left: H I integrated intensity contours at 1.6, 2.6, 5.2, 7.8, 12.9, 18.1, and 23.3 × 10²⁰ atoms cm⁻². The small galaxy within the easternmost H I contour extension is J114229.18+200713.7. Other details are per Fig. A1.

subcluster core. SDSS J114250.97+202631.8 has its highest column density H I (1.2 × 10²¹ atoms cm⁻²) detected 10.6 ± 2.9 arcsec (4 kpc) NW of the optical centre. As noted in Section 2, H I in this galaxy was detected beyond the FWHP of the VLA primary beam and there is no AGES spectrum available for this galaxy so its H I properties are more uncertain than for the other C-array LTGs.

CGCG 097−087: this is one of the best studied galaxies in the cluster, with our previous VLA D-array observations (Paper I) revealing a long diffuse ∼70 kpc H I tail which has H α and radio continuum counterparts (Boselli et al. 1994; Gavazzi et al. 1995, 2001a; Yagi et al. 2017). As noted in Section 3, the VLA C-array (Fig. A7) only maps the high column density regions in the VLA D-array map, but resolves its H I maximum into two distinct maxima SE and NW of the optical centre. The principal H I maxi-

mum (∼11:43:49.6 + 19:57:58) is projected ∼10.9 arcsec (4.5 kpc) SE of the optical centre and *Spitzer* 4.5-µm maxima. The secondary H I maximum (∼11:43:47.4 +19:58:28) lies ∼71 arcsec (29 kpc) NW of the optical centre and beyond the optical disc. There are two bright star-forming clumps at this position, with 4.5 µm and H α counterparts, possibly tracing *in-situ* star formation within the stripped gas. Both C-array H I maxima have counterparts in a VLT–MUSE¹⁹ H α image (Consolandi et al. 2017). Kinematically, the two maxima are quite distinct. The H I surrounding the SE maximum ($V_{H I} \sim$6520 km s⁻¹) shows a clear rotation signature across the
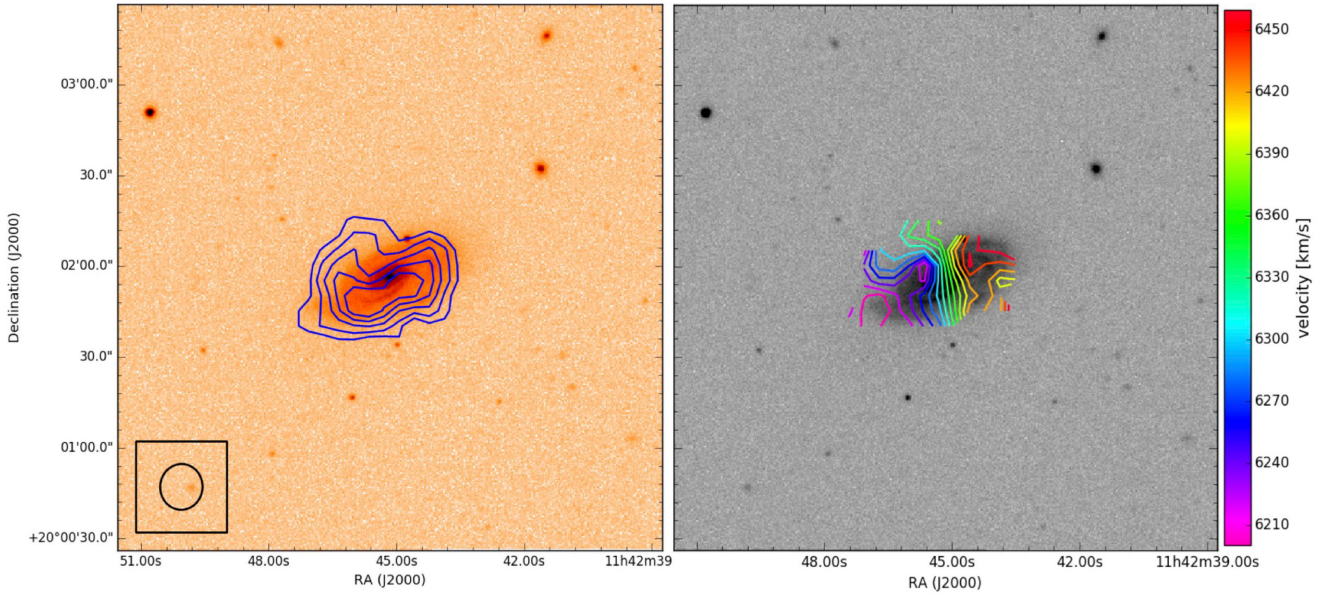
_____
¹⁹ The Multi Unit Spectroscopic Explorer.

Figure A5. CGCG 097−072, left: H I integrated intensity contours at 1.6, 2.6, 3.9, 5.2, and 6.5 × 10²⁰ atoms cm⁻². Other details are per Fig. A1.
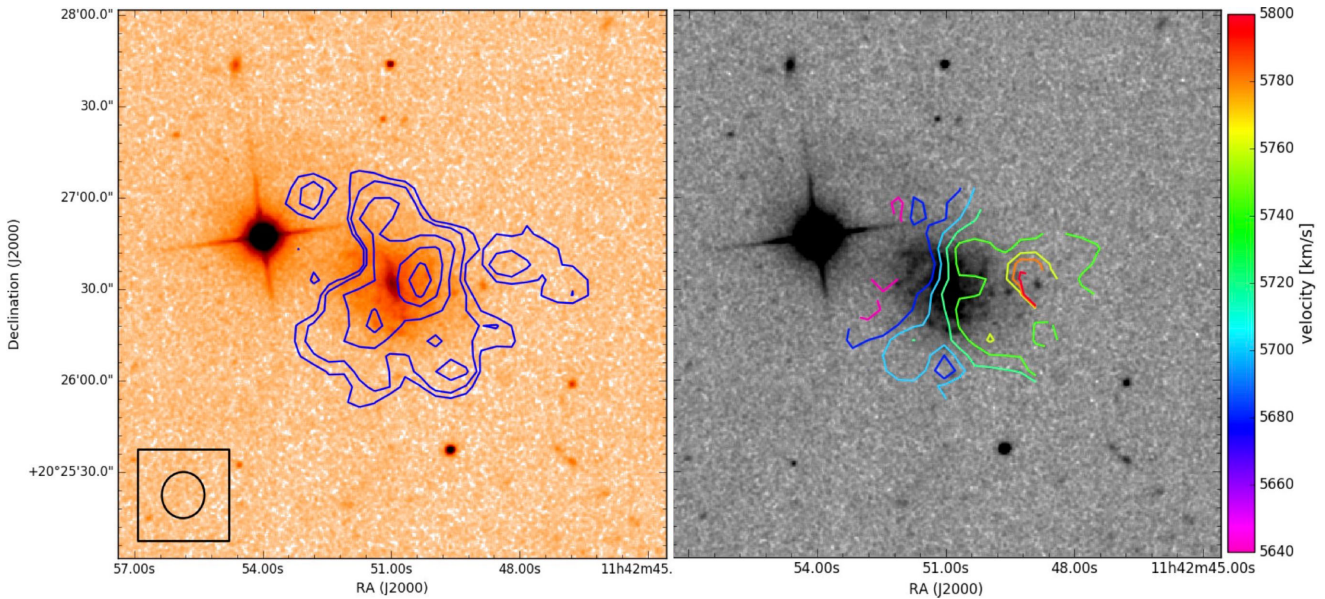

Figure A6. SDSS J114250.97+202631.8, left: H I integrated intensity contours at 1.6, 2.6, 5.2, 7.8, and 10.4 × 10²⁰ atoms cm⁻². Other details are per Fig. A1.

optical disc with the changing angle of the isovelocity contours indicating the H I disc is warped. This contrasts with the H I around the NW H I maximum, $V_{H I}$ ∼6880 km s⁻¹, which has a much shallower velocity gradient and less regular kinematics, probably reflecting turbulence in the H I displaced from the H I disc. Fig. A8 shows the H I position–velocity (PV) cut (PA = 135°) and the H I PV diagram centred on the galaxy's optical centre. Immediately, north of the optical centre and between H I maxima, the isovelocity contours are compressed with the velocity rising ∼200 km s⁻¹ over a projected distance of ∼10 arcsec (4 kpc). This is the position where (Gavazzi et al. 2001a) reported a ∼200 km s⁻¹ jump in Hα velocities. The MUSE Hα and [NII] emission maps show twin tails originating from a companion galaxy, CGCG 097−087N (projected 30 arcsec to the NE), and extending into the CGCG 097−087 H I velocity

jump region. This and an asymmetrically low H I column density feature extending to the optical centre from the SW supports a scenario in which CGCG 097−087N has made a passage from the SW through CGCG 097−087s H I disc as proposed in Consolandi et al. (2017). Unfortunately, our H I velocity coverage does not extend to the velocity of CGCG 097−087N. However, CGCG 097−087 is also undergoing strong ram-pressure stripping so it remains unclear to what extent the tidal interactions proposed in Consolandi et al. (2017) or in Gavazzi et al. (2001a) and Amram et al. (2002), account for the displacement of the large mass of H I now surrounding the NW H I maximum and the H I tail. Low-velocity (≲300 km s⁻¹) tidal interactions are capable of displacing large fractions of an interacting pair's H I beyond their optical discs (Sengupta et al. 2013, 2015), but in this case the companion is much less massive and the
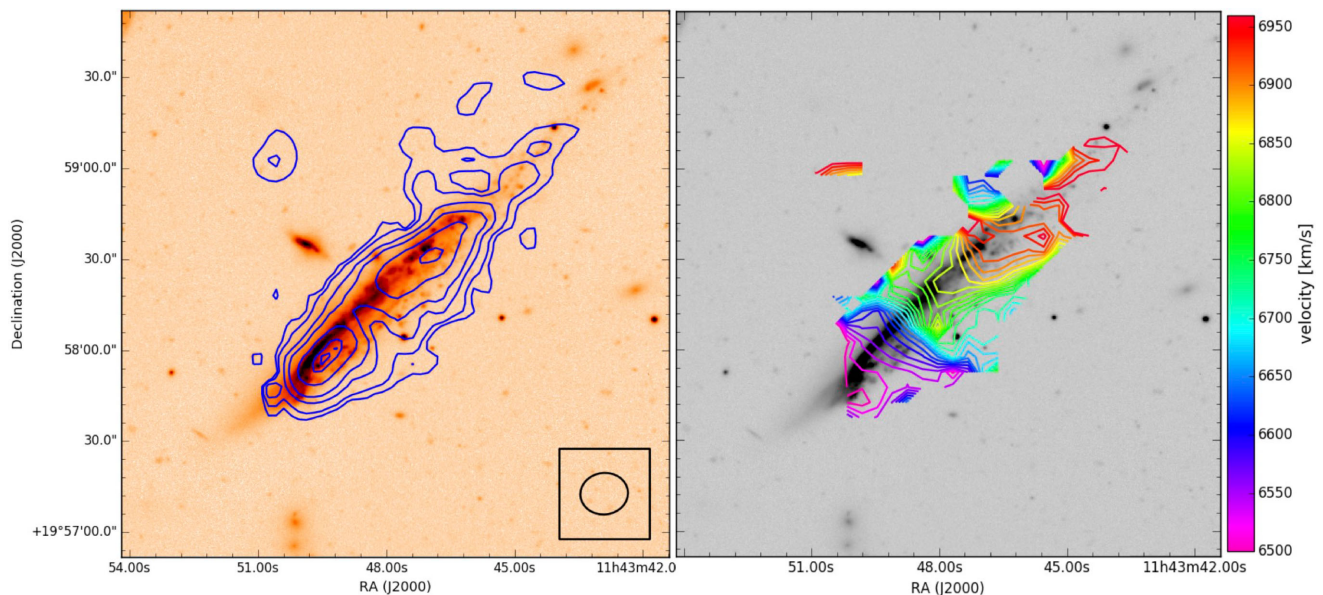
Figure A7. CGCG 97−087, left: H I integrated intensity contours at 1.7, 2.9, 5.8, 8.7, 14.4, 20.2, and 21.7 × 10^{20} atoms cm^{-2}. The background for both maps is a Canada–France–Hawaii Telescope *u*-band image. Other details are per Fig. A1.
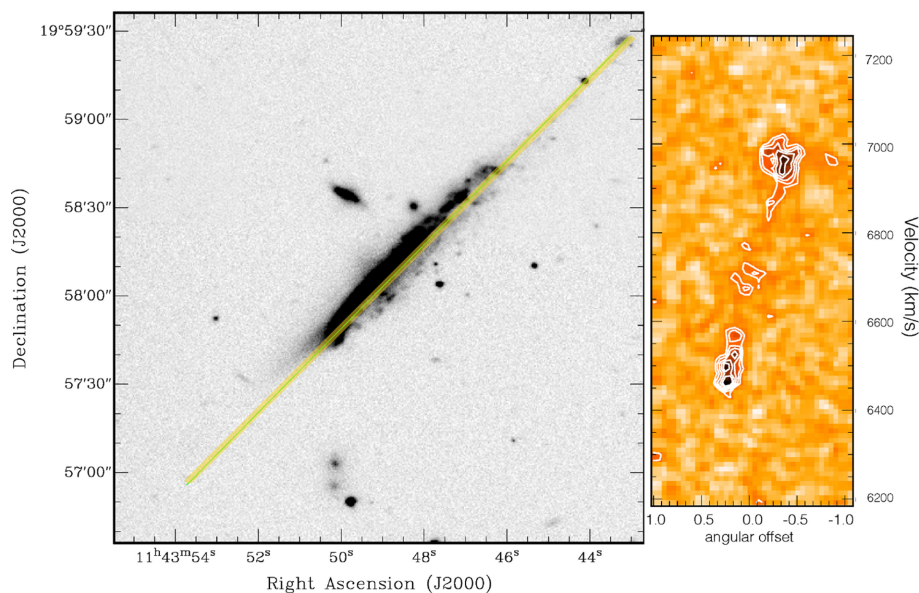

Figure A8. CGCG 97−087, left: SDSS *g*-band image illustrating the direction along which the position–velocity (PV) diagram was taken (PA = 135 °). Right: H I PV diagram PA = 135 °. Negative angular offsets (arcminutes) in the PV diagram are northwest of the optical centre and positive are to the southeast.

$\sim$800 km s^{-1} velocity separation (Consolandi et al. 2017) suggests a high-velocity low impact encounter.

CGCG 097−091: to a first-order CGCG 097−091 presents a symmetric H I disc. The highest column density H I (13 × 10^{20} atoms cm^{-2}) is well aligned in projection with the optical centre, although the low H I column density disc edge extends further to the south and the east than north and west. The closed isovelocity contours in the velocity field (Fig. A9, right-hand panel) indicates the H I disc is asymmetrically warped E and W of the optical centre. Together, the H I morphology and kinematics suggest the H I disc has suffered a recent weak perturbation. The WISE 3.4 μm image is consistent with a symmetric unperturbed old stellar disc.

CGCG 097−102: H I is projected against the optical discs of both members of this pair, CGCG 097−102N and CGCG 097−102S (Fig. A10). There is an apparent H I bridge/tail joining the pair, although the H I detection in this feature where it is projected against CGCG 097−102S, is only at the 3 σ level. CGCG 097−102N displays a quite irregular H I morphology with the column density maximum (5.1 × 10^{20} atoms cm^{-2}) offset 11.1 ± 2.9 arcsec (4.6 kpc) W of the optical centre and projected near the optical disc edge. The H I morphology of CGCG 097−102N is severely skewed to the S and W of the optical centre. The velocity field for CGCG 097−102N, right-hand panel of the figure, shows an overall rotating disc pattern. But the changing angle of the isovelocity contours indicates a strongly warped disc, with the change in angle of the contours being
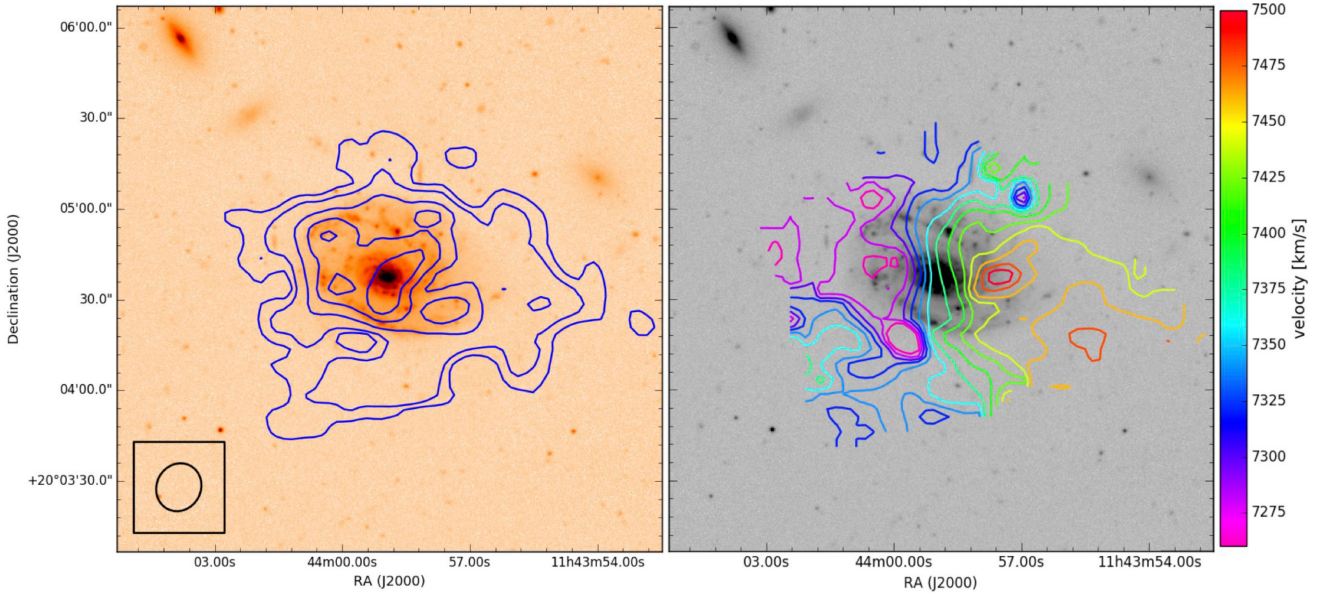
Figure A9. CGCG 97−091, left: H I integrated intensity contours at 1.6, 2.7, 5.4, 8.1, and 10.8 × 10^{20} atoms cm^{-2}. Other details are per Fig. A7.
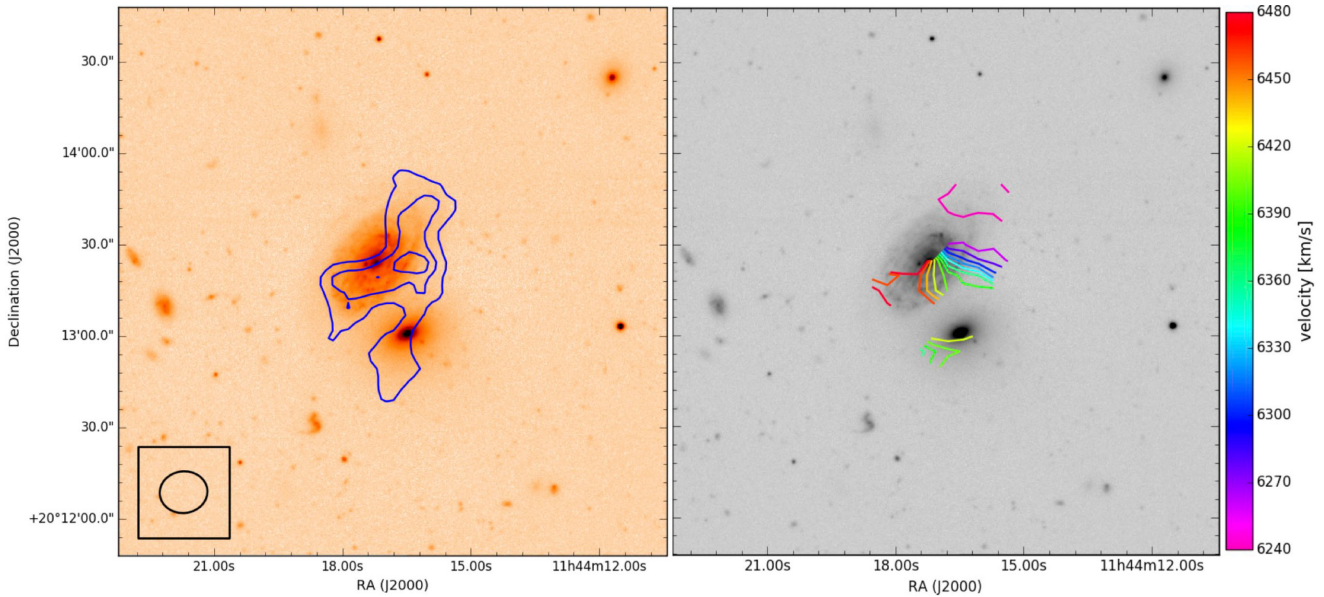

Figure A10. CGCG 97−102N ,left: H I integrated intensity contours at 1.7, 2.9, and 4.0 × 10^{20} atoms cm^{-2}. Other details are per Fig. A7.

greatest in the H I velocity range of the H I bridge/tail projected against CGCG 097−102S, i.e. $V \sim$ 6380–6460 km s^{-1}. The H I velocities of the H I projected against the CGCG 097−102S optical disc do not show a rotation pattern. This, the A_{flux} for CGCG 097−102N and the classification of CGCG 097−102S as an elliptical (NED) suggests the H I in the bridge projected against CGCG 097−102S has been tidally stripped from CGCG 097−102N by an interaction between the pair. A tidal interaction scenario is supported by evidence that the CGCG 097−102N molecular disc is also perturbed (Paper III). The edges of the optical discs are projected against each other and the optical velocities of the pair from NED are CGCG 097−102N (6368 ± 14 km s^{-1}) and CGCG 097−102S (6364 ± 9 km s^{-1}) give a difference of only

4 km s^{-1}. The CAS[20] (Conselice 2003) asymmetry parameter for CGCG 097−102N derived from an SPM[21] *J*-band image was 1.22 is in the domain of disturbed objects and provides evidence that the old stellar disc of CGCG 097−102N is perturbed in the SE, supporting the tidal interaction scenario (Venkatapathy et al. 2017).

CGCG 097−121 is an Sab galaxy projected ∼14.9 arcmin (370 kpc) from the NW subcluster core. Although there is an unusual structure in the inner optical disc, smoothed *Spitzer* 3.6- and 4.5-µm images show the morphology of the outer disc to be rather

---

[20] Concentration (C), asymmetry (A), and clumpiness (S) parameters.
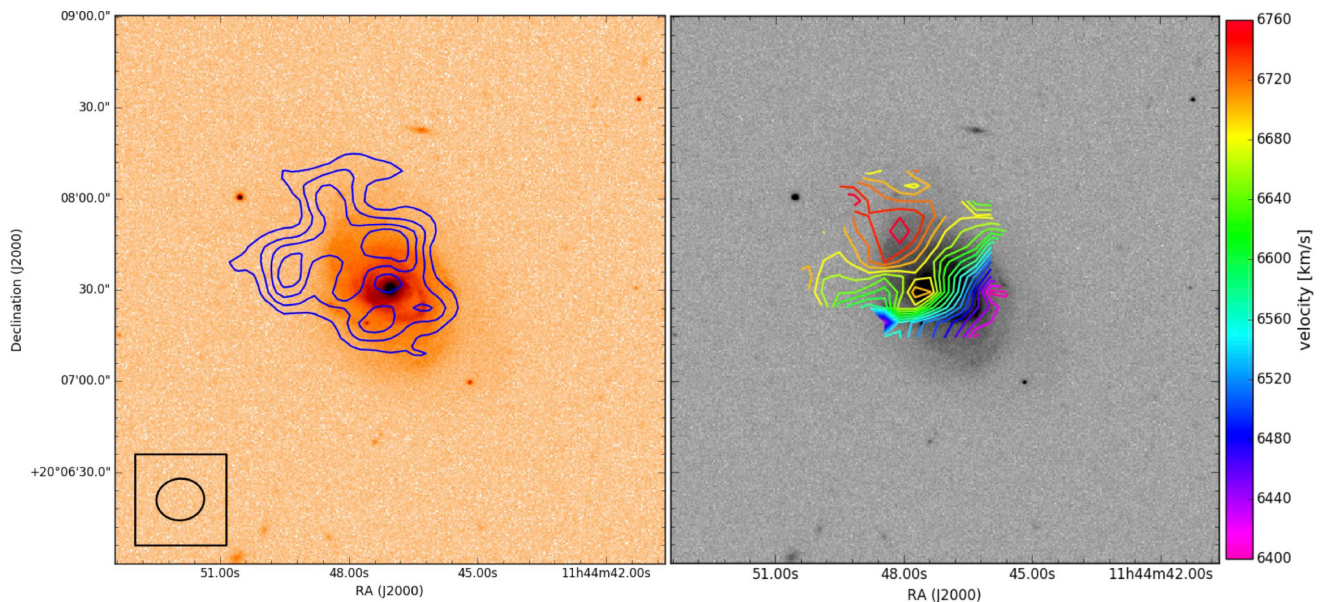[21] Observatorio Astronómico Nacional, San Pedro Mártir, Mexico.

Figure A11. CGCG 97−121, left: H I integrated intensity contours at 1.7, 2.9, 4.0, and 5.2 × 10²⁰ atoms cm⁻². Other details are per Fig. A1.
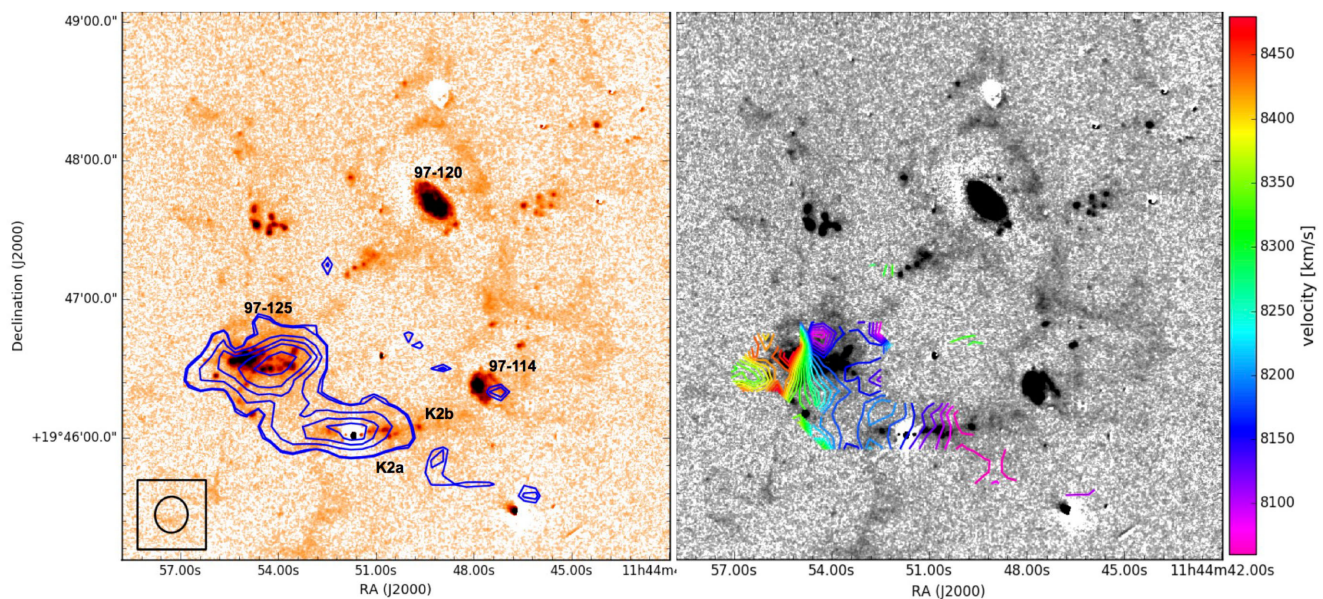

Figure A12. Blue infalling group (BIG). H I integrated intensity contours on deep Hα image (Cortese et al. 2006). Contours are at 1.8, 2.0, 4.0, 6.0, 8.0, and 12 × 10²⁰ atoms cm⁻². The projected positions of CGCG galaxies and H II regions (K2a and K2b) are also indicated on the integrated H I map. Other details are per Fig. A1.

symmetric, indicating the old stellar population there is unperturbed. This galaxy has an H I deficiency of 0.4 (Table 2) with the H I in the SE truncated ∼30 arcsec (12 kpc) inside the optical disc. The highest column density H I (6.4 × 10²⁰ atoms cm⁻²) is projected ∼13.6 arcsec (6 kpc) north of the optical centre and near the northern edge of the optical disc (Fig. A11). The H I velocity field (Fig. A11, right-hand panel) and $A_{\text{flux}} = 1.92 \pm 0.08$ show the H I kinematics are consistent with an ongoing interaction which is significantly perturbing the H I disc. The galaxy is also deficient in molecular gas, H₂ deficiency ∼0.48 (Paper III). The FUV and NUV (*GALEX*) images show a broad low surface brightness linear feature extending out to the northern edge of the optical disc and the 3σ H I contour.

The unperturbed old stellar disc, highly perturbed H I and gas deficiencies are all signatures expected from ram-pressure stripping. But as discussed in (Paper IV) such a large offset of highest column density H I in a spiral with its M* mass is not expected from simple ram-pressure stripping models, which predict only moderate P_{ram} ∼8 × 10¹² dyne cm⁻² at the projected position of the galaxy for a V_{rel} of 1000 km s⁻¹.

BIG compact group: BIG is projected near the centre of the SE subcluster but has mean optical velocity, <V_{opt}>, of 8230 km s⁻¹, which is ∼1750 km s⁻¹ higher than the <V_{opt}> for A1367 (Sakai et al. 2002; Cortese et al. 2006). The Hα image, fig. 2 in Cortese et al. (2006), shows spectacular Hα emission from tails tracing
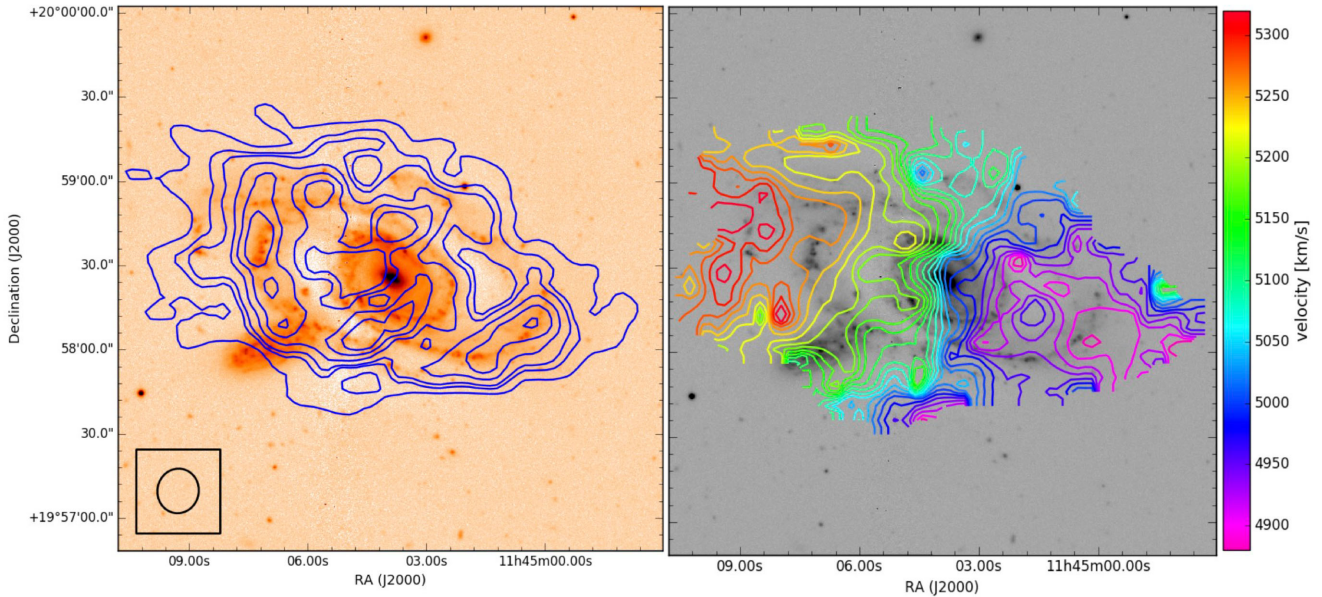
Figure A13. CGCG 97−129, left: H I integrated intensity contours at 1.6, 4.1, 5.4, 8.2, 10.9, and 13.6 × 10²⁰ atoms cm⁻². Other details are per Fig. A7.
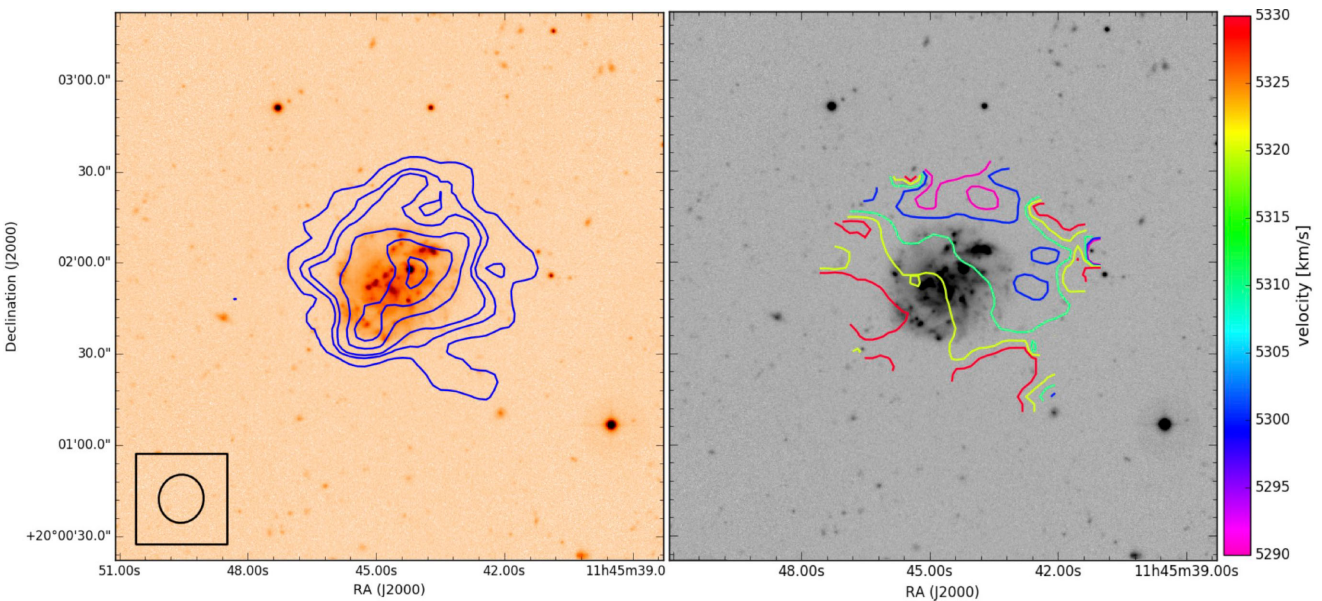

Figure A14. CGCG 97−138, left: H I integrated intensity contours at 1.6, 4.1, 5.4, 8.2, 10.9, and 13.6 × 10²⁰ atoms cm⁻². The separation between contours in the velocity field is 20 km s⁻¹. Other details are per Fig. A7.

interaction debris within the group. Fig. A12 shows the H I in the easternmost group member in the figure (CGCG 097−125) is highly perturbed with its H I column density maximum off-set 14.4 ± 2.9 arcsec (6 kpc) E of the optical centre. Strikingly CGCG 097−125 has a broad ∼80 arcsec (33 kpc) long H I tail curving to the SE. This tail contains a large H I mass (K2 in the Cortese et al. 2006 figure), near the position of a bright foreground star. The Cortese figure shows the eastern H I tail CGCG 097−125 has an H α counterpart which extends beyond the H I tail to the eastern side of the blue LTG, CGCG 097−114. The H I velocity field shows the H I velocity falling along the H I tail from 8277 ± 18 km s⁻¹ at the CGCG 097−125 column density maximum to ∼8100 km s⁻¹ at K2 ($V_{opt} \sim 8075$ km s⁻¹ at K2a). An H I clump is detected 10.4 arcsec (4 kpc) E of the CGCG 097−114 optical centre with

a $V_{HI} = 8451 \pm 20$ km s⁻¹. CGCG 097−114 emits strongly in H α and has $V_{opt} = 8425$ km s⁻¹. Our H I velocities for CGCG 097−114, CGCG 097−125 and K2 are in good agreement with those from the WSRT[22] (Sakai et al. 2002). This and the optical velocity of knot K2b (8309 km s⁻¹) suggests a tidal bridge between CGCG 097−125 and CGCG 097−114 forms an arc in velocity space reaching its minimum velocity at K2. BIG is projected ∼11 arcmin from the strong continuum source 3C264, making continuum subtraction in this field particularly difficult. Incomplete continuum subtraction is the most likely reason for the VLA C-array H I flux for BIG being higher than from AGES, see Table 2. For this reason, the first

---

[22] Westerbork Synthesis Radio Telescope.

contour in the BIG H I map is drawn at 4.5σ rather than at 3σ as in the other H I maps. Yagi et al. (2017) report an $\sim$300 kpc Hα tail emanating from BIG, which suggests that gas debris from tidal preprocessing interactions is in the process of being removed from the compact group by ram-pressure stripping.

CGCG 097−0129W: this large barred Sb spiral has a $D_{25} \approx$ 2 arcmin (50 kpc). The two impressive spiral arms emanating from the ends of the bar encircle the galaxy (Fig. A13). The H I maximum $(1.7 \times 10^{21}$ atoms cm$^{-2})$ is offset 32.4 ± 2.9 arcsec (13 kpc) E of the optical centre. A smaller cluster member CGCG 097−129E is projected at the eastern edge of the optical disc but its optical velocity is 2455 km s^{-1} higher than CGCG 097−129W. Smoothed *Spitzer* 3.6- and 4.5-μm images suggest the old stellar disc of CGCG 097−129W, at the radius of the encircling optical arms, is to a first-order symmetric. The H I disc extends $\sim$30 arcsec (12 kpc) beyond the optical disc both to the NE and SW. Overall, the H I velocity field (Fig. A13) reflects a rotating disc. However, the kinematics are quite perturbed and the closed isovelocity contours near the disc edges and changing isovelocity contour angles indicate an asymmetrically warped H I disc.

CGCG 097−138: this blue (SDSS $g - i = 0.82$) galaxy displays a rapid rise in H I column density in the SE where the edge of the H I disc is truncated closer to the optical disc edge compared to the north and west. The H I intensity maximum $(1.4 \times 10^{21}$ atoms cm$^{-2})$ is located close to the NW optical disc edge. The small H I W_{20} value of 64 ± 3 km s^{-1} and the velocity field isovelocity contours (Fig. A14), which shows a systematic gradient in the SE–NW direction, suggest we are viewing the H I disc at low inclination angle (36.3° per Hyperleda for the optical disc). There are NUV *(GALEX)* maxima at the optical centre and $\sim$10 arcsec (4 kpc) NW of a bright $m_{\mathrm{g}} = 16.4$ star projected in front of the optical disc. Both NUV maxima have counterparts in the Hα GOLDMine image. A smoothed *H*-band image (GoldMine) shows the disc edge to be quite irregular. It is not clear whether the *H*-band morphology is the result of a recent interaction or the inherent morphology of the galaxy.

APPENDIX B: DATA REDUCTION: INDIVIDUAL FIELDS

B1 Field B (day 5 observations)

This field (Fig. 1), centred near the cluster centre, has a significant spatial overlap with the SE of Field D. Two discrete velocity ranges were observed using IF1 and IF2. IF1 covered a range of 7978–8511 km s^{-1} with central velocity set to the Blue Infalling Group's (Cortese et al. 2006) mean velocity. The observations from this IF were combined in the *uv*-plane with C-array observations from 2002 December at the same position and reported in Paper I. The combined data were used to produce an image cube with 48 channels covering the velocity range from 7978 to 8511 km s^{-1} with a velocity width of 11 km s^{-1} per channel. The rms per channel of the combined cube was $\sim$0.26 mJy. For the combined cube, the

equivalent H I mass detection threshold is $\sim 5.2 \times 10^7$ M$_{\odot}$ (corresponding to 3σ in two consecutive 11 km s^{-1} channels). This is equivalent to a column density sensitivity for emission filling the beam of 1.7×10^{19} cm^{-2}.

IF2 produced a cube with a velocity range of 4836–5358 km s^{-1}. For this cube, the equivalent H I mass detection threshold is $\sim 5.7 \times 10^7$ M$_{\odot}$ (corresponding to 3σ in two consecutive 11 km s^{-1} channels). This is equivalent to a column density sensitivity for emission filling the beam of 1.9×10^{19} cm^{-2}.

B2 Field C (day 1 and 2 observations)

Field C (Fig. 1) is centred $\sim$25 arcmin NW of the NW cluster centre (Cortese et al. 2004). It was planned that on day 1 two IFs would cover two adjacent 500 km s^{-1} velocity ranges with the similar set up on day 2 to extend the velocity range by a further 1000 km s^{-1}. The intention was to combine the cubes to produce a consolidated cube with a contiguous 2000 km s^{-1} range. Unfortunately because of a telescope scheduling error, 7 h of the 9 h of planned day 2 observation time was applied to re-observing the day 1 velocity range. As a result, there were no H I detections in the day 2 cube. However, the day 1 (lower velocity range) observations were correspondingly deeper than planned and combining IF1 and IF2 produced an image cube with 100 channels covering the velocity range from 5504 to 6565 km s^{-1} with a velocity width of 11 km s^{-1} per channel. The rms per channel of the combined cube was $\sim$0.22 mJy. For the combined cube, the equivalent H I mass detection threshold is $\sim 4.4 \times 10^7$ M$_{\odot}$ (corresponding to 3σ in two consecutive 11 km s^{-1} channels). This is equivalent to a column density sensitivity for emission filling the beam of 1.6×10^{19} cm^{-2}.

The unsuccessful day 2 observation targets included CGCG 097−062. However, the NRAO VLA archive contains VLA C-array H I observations for this galaxy. We retrieved this archive data and reduced it with AIPS using the standard reduction procedure. For consistency, the continuum subtraction technique applied for our own C-array data was also applied to the CGCG 097−062 H I data. We include CGCG 097−062 in our analysis of galaxies with resolved H I.

B3 Field D (day 3 and 4 observations)

Field D (Fig. 1) is centred $\sim$14 arcmin NE of the NW cluster centre (Cortese et al. 2004). Cubes were produced from observations of this field with the following discrete velocity ranges 7091–7463 km s^{-1} (day 3 IF1–52 channels), 4825–5369 km s^{-1} (day 3 IF2–52 channels), and 6194–7236 km s^{-1} (day 4 IF1 and IF2–98 channels). The rms per channel of the cubes were $\sim$0.34, 0.35, and 0.25 mJy, respectively, with their column density and mass sensitivity limits shown in Table 1.

This paper has been typeset from a TEX/LATEX file prepared by the author.